Long-baseline horizontal radio-frequency transmission through polar ice

Allison, P.[2,3] Archambault, S.[4] Beatty, J.J.[2,3] Besson, D.Z.[1,7]
Chen, C.C.[8] Chen, C.H.[8] Chen, P.[8] Christenson, A.[5] Clark,
B.A.[2,3] Clay, W.[10] Connolly, A.[2,3] Cremonesi, L.[9] Deaconu, C.[10]
Duvernois, M.[5] Friedman, L.[6] Gaior, R.[4] Hanson, J.[2,3] Hanson,
K.[5] Haugen, J.[5] Hoffman, K.D.[6] Hong, E.[2,3] Hornhuber, C.[1]
Hsu, S.Y.[8] Hu, L.[8] Huang, J.J.[8] Huang, M.-H. A.[8] Hughes, K.[10]
Ishihara, A.[4] Karle, A.[5] Kelley, J.L.[5] Khandelwal, R.[5] Kim,
M.-C.[4] Kravchenko, I.[11] Kruse, J.[11] Kurusu, K.[4] Kuwabara, T.[4]
Latif, U.A.[1] Laundrie, A.[5] Li, C.-J.[8] Liu, T.-C.[8] Lu, M.-Y.[5]
Madison, B.[1] Mase, K.[4] Meures, T.[5] Nam, J.[4] Nichols, R.J.[9]
Novikov, A.[1,7] Nozdrina, A.[1] Oberla, E.[10] Pan, Y.[13] Pfendner,
C.[2,3] Relich, M.[3] Sandstrom, P.[5] Seckel, D.[13] Shiao, Y.S.[8]
Shultz, A.[1] Smith, D.[10] Song, M.[6] Torres, J.[2,3] Touart, J.[6]
Varner, G.S.[14] Vieregg, A.[10] Wang, M.Z.[8] Wang, S.H.[8] Wissel,
S.[15] Yoshida, S.[4] Young, R.[1] Jordan, T.[12]

[1]Dept. of Physics and Astronomy, Univ. of Kansas, Lawrence, KS, USA

[2]Dept. of Physics, The Ohio State University, 191 West Woodruff Avenue, Columbus, OH, USA

[3]Center for Cosmology and Astro-Particle Physics, The Ohio State University, 191 West Woodruff Avenue, Columbus, OH, USA

[4]Dept. of Physics, Chiba University, Tokyo, Japan

[5]Dept. of Physics and Wisconsin IceCube Particle Astrophysics Center, University of Wisconsin, Madison, WI, USA

[6]Dept. of Physics, Univ. of Maryland, College Park, MD, USA

[7]National Research Nuclear University, Moscow Engineering Physics Institute, Moscow, Russia

[8]Dept. of Physics, Grad. Inst. of Astrophys., & Leung Center for Cosmology and Particle Astrophysics, National Taiwan Univ., Taipei, Taiwan

[9]Dept. of Physics and Astronomy, Univ. College London, London, United Kingdom

[10]Dept. of Physics, University of Chicago, Chicago, IL, USA

[11]Dept. of Physics and Astronomy, Univ. of Nebraska-Lincoln, NE, USA

[13]Dept. of Physics and Astronomy, Univ. of Delaware, Newark, DE, USA

[14]Dept. of Physics and Astronomy, Univ. of Hawaii, Manoa, HI, USA

[15]Dept. of Physics, California Polytechnic State University, San Luis Obispo, CA, USA

E-mail: dbesson@ku.edu; dvbesson@mephi.ru

Abstract. We report on analysis of englacial radio-frequency (RF) pulser data received over horizontal baselines of 1–5 km, based on broadcasts from two sets of transmitters deployed to depths of up to 1500 meters at the South Pole. First, we analyze data collected using two RF bicone transmitters 1400 meters below the ice surface, and frozen into boreholes drilled for the IceCube experiment in 2011. Additionally, in Dec., 2018, a fat-dipole antenna, fed by one of three high-voltage ($\mathcal{O}(1$ kV$)$), fast ($\mathcal{O}(1$-5 ns risetime$)$) signal generators was lowered into the 1700-m deep icehole drilled for the South Pole Ice Core Experiment (SPICE), approximately 3 km from the geographic South Pole. Signals from transmitters were recorded on the five englacial multi-receiver ARA stations, with receiver depths between 60–200 m. From analysis of deep transmitter data, we estimate: i) the range of refractive index profiles of Antarctic ice with depth allowed by our measurements, ii) due to birefringence, a time difference between arrival times for vertically polarized vs. horizontally polarized signals (per km) for horizontally propagating signal, and iii) for the first time, the attenuation length for electromagnetic signals in the radio-frequency regime broadcast horizontally (rather than reflected vertically from bedrock). We additionally present data suggesting anomalous ice propagation effects, and contrary to expectations for a transport medium with a smoothly varying refractive index profile.

Our results imply negligible uncertainty in overall neutrino detection volume due to refractive index uncertainties. Our birefringence time-difference measurements are fit to the functional form $\delta_t(H - V)[\text{ns/km}] = a\cos\theta + b$, with H/V the signal arrival times for the horizontally/vertically polarized EM signal components, and θ the opening angle in the horizontal plane between the signal propagation direction and the local ice flow direction, extracting a=8.3±1.3 ns/km, and b=-8.6±0.9 ns/km (errors combined statistical and systematic), allowing a ∼15% range estimate for future measurements of in-ice neutrino interactions. Finally, we find attenuation length values clustering around 1.5 km, with measurements from the bicone transmitters yielding $L_{atten} = 1.43 \pm 0.25 \pm 0.37$ km. Taken together, these measurements support cold polar ice as a near-optimal platform for ultra-high energy neutrino detectors.

Contents

1 Introduction

Although originally purposed for radio-wave detection of ultra-high energy neutrinos interacting in cold polar ice via the Askaryan effect[1–3], the RICE[4], ANITA[5], ARA[6] and ARIANNA[7] experiments have also realized extensive radioglaciological programs[8–13]. Precise, and complete characterization of ice RF dielectric properties is important to optimizing both the layout as well as the trigger for existing, as well as planned neutrino detection experiments. Previous studies have measured the imaginary and real portions of the complex dielectric permittivity[8, 14, 15], based primarily on vertical radar echoes measured through South Polar ice, consistent with the typical, and logistically simplest, bistatic (i.e., nearly co-located receiver and transmitter) geometry. RF transmissions along a primarily horizontal chord require in-ice transmitter (Tx) and receiver (Rx) km-scale horizontal separations, and present a considerably greater logistical challenge. We herein detail our observations of horizontally-propagating radio-frequency signals from transmitters at depths up to 1400 meters in South Polar ice, and quantify, where possible, the associated permittivity.

1.1 Ice-based neutrino detectors

The ARA, ARIANNA and ANITA experiments were designed to discover neutrinos at energies comparable to the ultra high energy charged cosmic rays (UHECR; $E > 10$ PeV) detected by surface detector arrays such as the Telescope Array[16] and the Auger Experiment[17]. Such neutrinos carry unique information from corners of the Universe otherwise inaccessible to charged UHECR astroparticle physics, owing to the GZK-effect[18–20]. The experimental technique is based on measurement of radio-frequency coherent Cherenkov radiation emitted by the particle shower produced by an in-ice neutrino-molecular interaction[1–3]. As part of the initial ARA receiver calibration plan one decade ago, three 'deep' radio-frequency pulsers were deployed during the last year (2011-12) of ice-hole drilling for the IceCube experiment at the 1–2 km depths typical of neutrino interactions. Two of these transmitters were deployed at z=−1400 meter depths in IceCube holes 1 (transmitter 'IC1S') and 22 (transmitter 'IC22S'), respectively. A third was deployed below the IceCube array in hole 1 ('IC1D') to a depth of 2400 meters, but failed shortly after initial operation. Deployment of six ARA receiver stations ("testbed" [2011], "A1" [2012], "A2"/"A3" [2013] and "A4"/"A5" [2017]), displaced 1-5 km horizontally from the IceCube array, allow study of radio signals propagating at primarily horizontal trajectories through the ice. Co-located with ARA station A5, the addition of a phased-array in the 2017-18 austral field season, with significantly lower signal thresholds[21] constitutes a powerful augmentation to both the physics, as well as glaciological reach of the ARA instrument.

1.2 Complex Dielectric Permittivity Measurements

Several permittivity measurements are accessible to ARA. Comparing the arrival time of received signals in the horizontally-polarized (HPol) to the vertically-polarized (VPol) receivers in an ARA station allows one to quantify possible polarization-dependence of electromagnetic wavespeed, aka 'birefringence'. Comparison of the relative signal strength observed in a near receiver station with a far receiver station permits extraction of the absorption, per unit length, of radio waves in ice, corresponding to the imaginary portion of the dielectric permittivity. Owing to the variable index-of-refraction with depth in the ice, RF rays will follow arcs between source and receiver, with, in general, both a direct ('D') as well as a refracted ('R') path allowed, as illustrated in Figure 1. (If the signal geometry is sufficiently vertical, the refracted ray reaches the surface before 'turning over' and is, in that case, more properly a reflected ray.) Such a time-delayed 'double pulse' signal constitutes an unambiguous signature for an in-ice neutrino interaction. Figure 2 illustrates the geometric similarity between the time-difference calibration measurements described herein and the sought-after neutrino signal.

If the horizontal range is known *a priori*, the 100-500 ns separation in arrival time between the D and R signals can also be used to discriminate between models for the refractive index variation n(z) with depth into the South Polar ice sheet. Alternatively, if the dependence of the time difference on range is known, a measured time difference can be used to infer the range to an in-ice source[13]. A smooth depth variation of n(z) also has an important consequence, namely, that there is a 'shadow zone' for which there are no solutions to Maxwell's Equations when both receiver and transmitter are located near, and slightly below the ice-air interface. In the Huygens picture, shadowing corresponds to a complete cancellation of all signal wavelets in this region. The extent of this shadow zone depends on both the lateral displacement of Tx and Rx, as well as their depths. For a typical ARA receiver depth of 180 meters, and a lateral displacement of 2 km (typical of the measurements presented herein), the
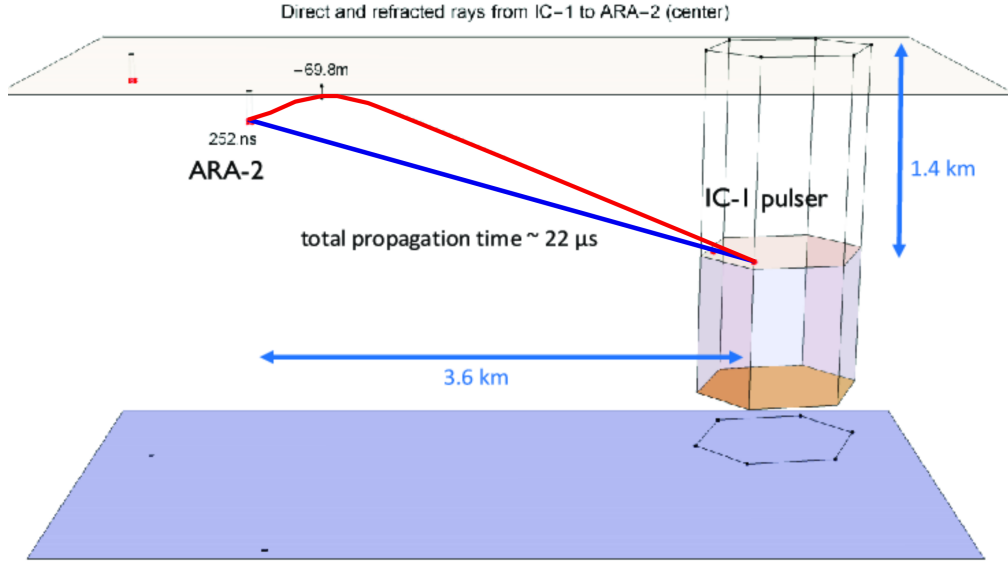
Figure 1. Trajectories of Direct and Refracted rays emitted from IceCube pulser IC1S and propagating to ARA Station 2. In this case, there is a 252 ns lag between the signal arrival at the 200-m deep ARA-2 receiver of the Refracted ray (red), which inflects at a depth of –69.8 m, relative to the Direct ray (blue). Additional dimensions/times are as shown in the Figure.
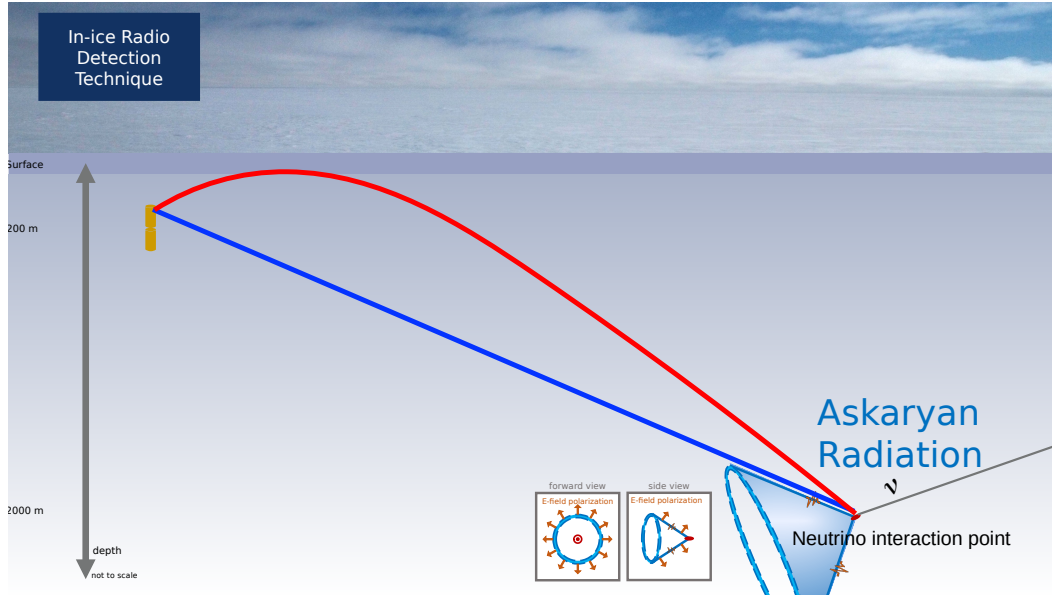
Figure 2. Modeled trajectories of Direct and Refracted rays emanating from the vertex of a Cherenkov cone, following an in-ice neutrino interaction. Note the similarity to the calibration signals illustrated in the previous Figure.

transmitter shadow zone extends downwards from the surface to approximately 500 meters transmitter depth. Recently, and somewhat unexpectedly, propagation of signals from within the shadow zone have been reported[22, 23], possibly linked to local (meter-scale) variations in the index-of-refraction profile and/or internal layering. As shown below, our data shows evidence for additional anomalies in radio-frequency propagation through South Polar ice.

1.3 SPICE core transmissions

We now outline the geometry and configuration for data-taking.

1.3.1 Ice cores and the SPICE core

The original glaciological goal of the South Pole Ice Core Experiment (SPICE)[24] was to measure, and also track changes in atmospheric chemistry, climate, and biogeochemistry over time, based on the measured properties of extracted cores. The SPICE core at South Pole is one of the few cores from the polar plateau and therefore fills in essential information between the Vostok[25], Dome C[26] and WAIS divide cores[27]. Measurements at $\sim$meter scales offer the opportunity to link macroscopic studies of RF propagation with the microscopic properties of ice crystals. On the molecular scale, H_2O molecules in the familiar ice-Ih phase self-order into a 6-fold rotationally symmetric lattice, with oxygen atoms at each of the planar hexagonal vertices. Locally, cm-scale ice grains are typically parameterized in terms of a 3-dimensional 'c'-axis, perpendicular to the hexagonal plane comprised by six ice molecules. The global orientation of the crystal ("COF", or Crystal Orientation Fabric) is generally referenced relative to vertical (by convention, defined as $\hat{z}$) and a horizontal direction – although coring devices thus far do not usually record azimuthal orientation, a reasonable ansatz aligns the x-axis with the local ice flow direction, which is generally known, and, aside from gravity, the only other symmetry-breaking stress in the ice. With those assumptions, one can then quantify the projections of the ice crystal orientation onto the (x, y, z) axes for each grain. Qualitatively, analysis of samples taken from multiple cores leads to a standard picture in which the c-axes increasingly rotate towards compressional axes (in this case, gravity) with depth. Quantifying the c-axis alignment in terms of ellipsoidal principal moments $< \hat{e}_1 >$ (parallel to ice flow), $< \hat{e}_2 >$ (perpendicular to ice flow) and $< \hat{e}_3 >$ (vertical, and coincident with $\hat{z}$), then, at ice depths to $\sim$500 meters, the ice fabric is largely randomly aligned ($< \hat{e}_1 > \approx < \hat{e}_2 > \approx < \hat{e}_3 >$). Over the next kilometer in depth, the locus of c-axes forms a 'girdle' through which the ice 'flows' as compressional effects become increasingly noticeable and the c-axis distribution favors the yz-plane ($< \hat{e}_1 > \approx 0; < \hat{e}_2 > \approx < \hat{e}_3 >$). At greater depths, the vertical gravitational stress increasingly rotates the c-axes to point directly along $\pm z$ ($< \hat{e}_1 > \approx < \hat{e}_2 > \approx 0; < \hat{e}_3 > \approx 1$). The birefringent asymmetry for flow parallel vs. perpendicular to ice flow is therefore roughly proportional to the asymmetry between $< \hat{e}_1 >$ and $< \hat{e}_2 >$. Note that the principal moments represent the eigenvectors of the orientation axes; the distribution of values around those eigenvectors is typically presented in the form of a Schmidt diagram[28].

1.3.2 South Pole University of Kansas Pressure Vessel Antenna (SPUNK PVA)

Design of the SPUNK transmitter antenna was tailored to match the 97-mm diameter of the SPICE core borehole, and the pressure of the estisol-240 drilling fluid environment into which the antenna was immersed. An aluminum fat-dipole antenna design based on the original RICE experimental model[4], with one of the two cylindrical halves also serving as a sealed pressure vessel and containing batteries and a custom, high-voltage transmitter, was

employed. As expected, the antenna broadcast efficiency improves when fully immersed in the estisol-240 (n∼1.42), as the intrinsic impedance of the dipole (∼72Ω for an ideal dipole in vacuum) approaches the 50Ω impedance of the cable used to convey the transmitter signal output to the antenna feedpoint. To ensure hermiticity, the feedpoint was itself flooded with epoxy to stand off the ambient hydrostatic pressure. A diagram of the SPUNK PVA, with a cut-away, is shown in Figure 3.

2 Data-taking

2.1 Set-up

Figure 4 illustrates the experimental layout during the eight day period (12/23/18–12/31/18, corresponding to Julian Days 358–365) over which SPUNK PVA pulsing occurred. Two surface horn antennas (designed and built by the Institute of Nuclear Research, Moscow) provided real-time monitoring on a surface oscilloscope of the emitted signals, and ensured that the pulser was active. Figure 5 shows a photograph of the experiment, just prior to lowering the SPUNK PVA into the SPICE core borehole.

2.2 Transmitter→Receiver Geometry

Since birefringence is linked to the local crystal orientation, the relative alignment of the receiver stations with respect to the transmitter is important for interpreting results. The geometry of the SPICE core (surveyed in the 2017-18 field season at 89.9889 S, 98.1596 W [or 89° 59' 20.168" S, 98° 09' 34.528" W][1] relative to the ARA stations is presented in Table 1 as well as Figure 6, including the distances d in meters between the centroid of a given ARA station (denoted "A1"–"A5", with the exception of the initial Testbed, as shown) and the transmitter source (measured relative to either the top of the SPICE core, or one of the deep pulsers co-deployed with the IceCube array in 2011-12, to a depth of 1400 m, on either IceCube String 1 or String 22). Vis-a-vis the later discussion of birefringence, the azimuthal angle ϕ between the line connecting the receiver to a given transmitter source and the local ice flow direction is also shown.

| Station	SPICE $d_{\mathsf{source}}/\phi_{source}/\phi_{ice\ flow}$	IC1S $d_{\mathsf{source}}/\phi_{source}/\phi_{ice\ flow}$	IC22S $d_{\mathsf{source}}/\phi_{source}/\phi_{ice\ flow}$
Testbed	(no data)	2463 m/-25°/23°	2199 m/-20°/29°
A1	1257 m/-30°/18°	2517 m/-4°/44°	2322 m/3°/53°
A2	2353 m/28°/76°	3729 m/27°/76°	3674 m/33°/82°
A3	3146 m/-12°/37°	4323 m/-2°/47°	4099 m/2°/50°
A4	3199 m/-49°/1°	3865 m/-32°/17°	3534 m/-30°/19°
A5	4164 m/43°/91°	5364 m/39°/88°	5377 m/43°/92°

Table 1. Lateral distances and azimuthal orientation relative to both the indicated sources, as well as local ice flow, with $\phi_{ice\ flow}$=0 defined as parallel to the local ice flow direction, for measurements described herein. We note that two of the ARA stations (A2 and A5) are oriented predominantly perpendicular to the local ice flow direction, while stations A1 and A4 are oriented predominantly parallel to the ice flow direction. Typical errors are estimated to be approximately one degree.

---

[1]We note that the local ice flow has magnitude ∼10 m per year, so the hole must be periodically re-surveyed, although the location relative to the ARA stations, which are co-moving, should remain approximately constant.
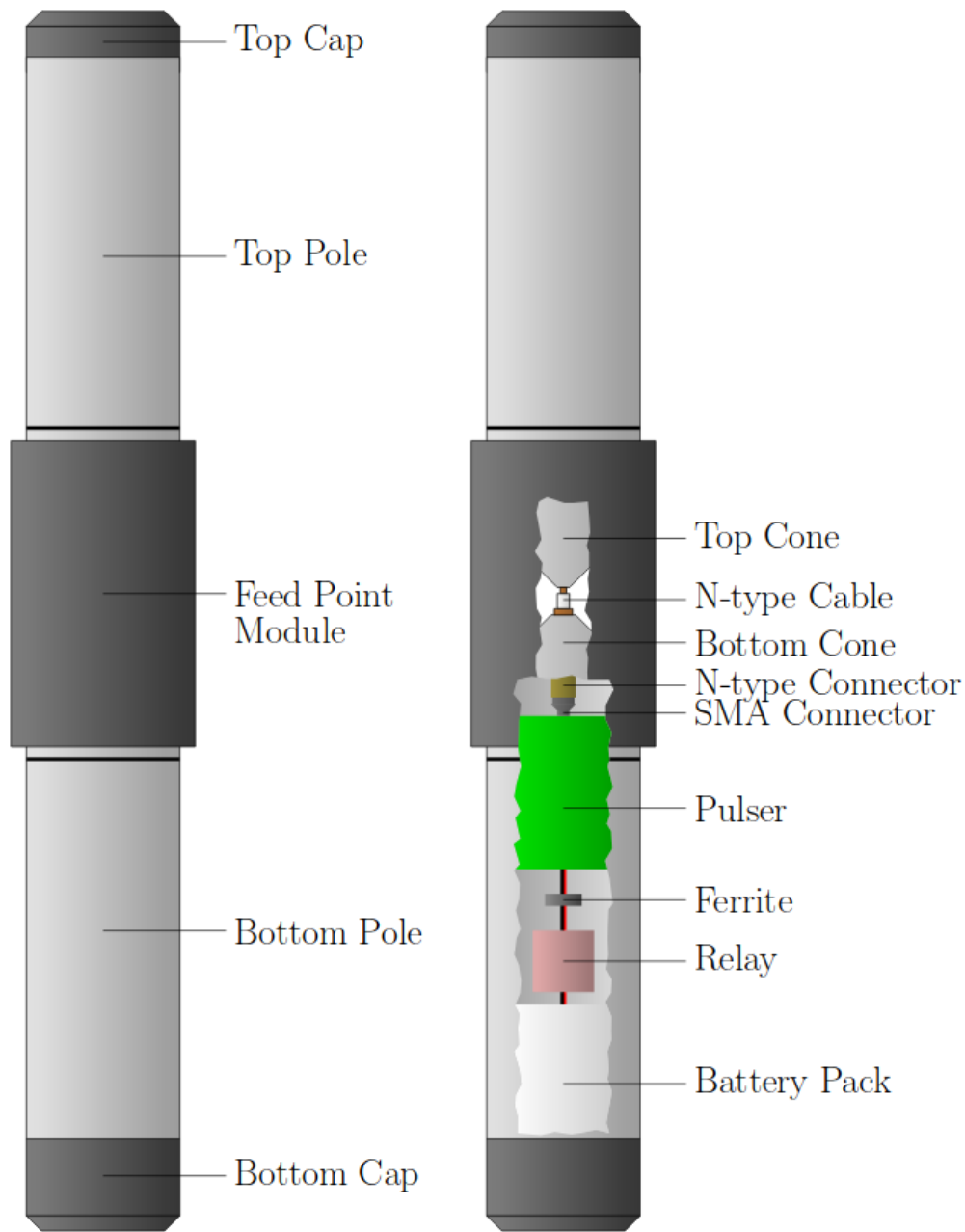
Figure 3. Pressure Vessel Antenna (aka "SPICE Pulser from UNiversity of Kansas", or SPUNK) used for broadcasts from the SPICE borehole. Vertical × horizontal dimensions of PVA are approximately 90 × 9 cm. Indicated in the figure are: i) Battery Pack used to power the ii) piezo, IDL or HVSP Pulser (in green), iii) Ferrite used to isolate Pulser from Relay, iv) Magnetically-sensitive relay (beige) allowing activation of unit after sealing, v) connection at feed point between Top and Bottom cones of dipole. Note that feed point is flooded with epoxy to stand off penetration from drilling fluid after immersion in SPICE core hole.
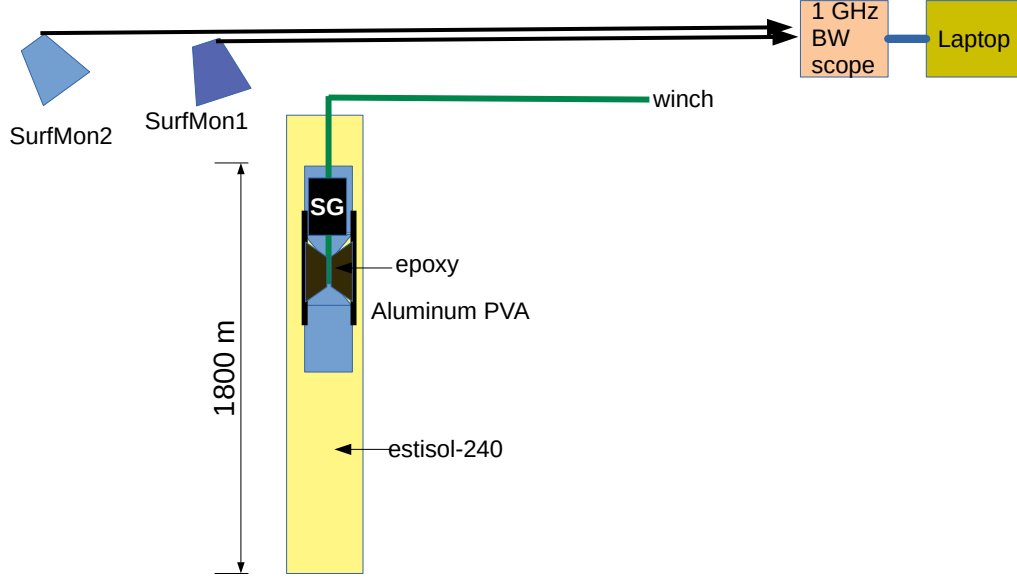
Figure 4. SPICE core pulsing configuration, showing the Pressure Vessel Antenna (PVA) immersed in estisol. Two surface horn antennas were used to verify real-time pulsing of the in-ice SPUNK PVA. Indicated in the Figure is the Signal Generator unit (comprising Pulser, Ferrite, Relay and Battery Pack from previous Figure). Winch controls only ascent/descent of PVA into estisol-240 drilling fluid, and has no power/communications functionality. To monitor Signal Generator in real-time, two surface monitor horn antennas (SurfMon1 and SurfMon2) are placed on surface approximately 5 meters and 50 meters, respectively, from SPICE core hole. Surface monitor signals are conveyed by LMR-400 cable to a battery-powered 1 GigaHertz bandwidth Agilent digital sampling oscilloscope, with data from the oscilloscope written to laptop.

The most detailed data at South Pole on the ice flow is provided by the IceCube experiment itself, who have measured the velocity field over a roughly one square kilometer scale. Local angular deviations from uniform flow of several degrees, over the km^2 measurement area covered, are not uncommon, and indicative of the angular systematic error for the values presented in Table 1.

Over a period of 6–8 hours,[2] the transmitter antenna was lowered into the SPICE borehole to an 1100–1700 depth, and then retracted back to the surface. Figure 7 illustrates the depth vs. time profile for the seven days over which data were taken. The three pulsers used include the piezo model used for the HiCal experiment[9, 29–31], and transmitters based on generating high-voltage across a spark gap ("HVSP"), as well as a fast high-voltage discharge generated by a transistor array ("IDL"); both of the latter two models include fast DC→DC converters in their design.

Since the SPUNK transmitter within the PVA upper dipole chamber was powered by battery, after initial activation at the surface, the transmitter broadcast continuously over the entirety of the transmitter drop. To facilitate offline identification of pulses from the SPUNK pulser, with the exception of the mechanically-activated piezo-electric transmitter, which ex-

---
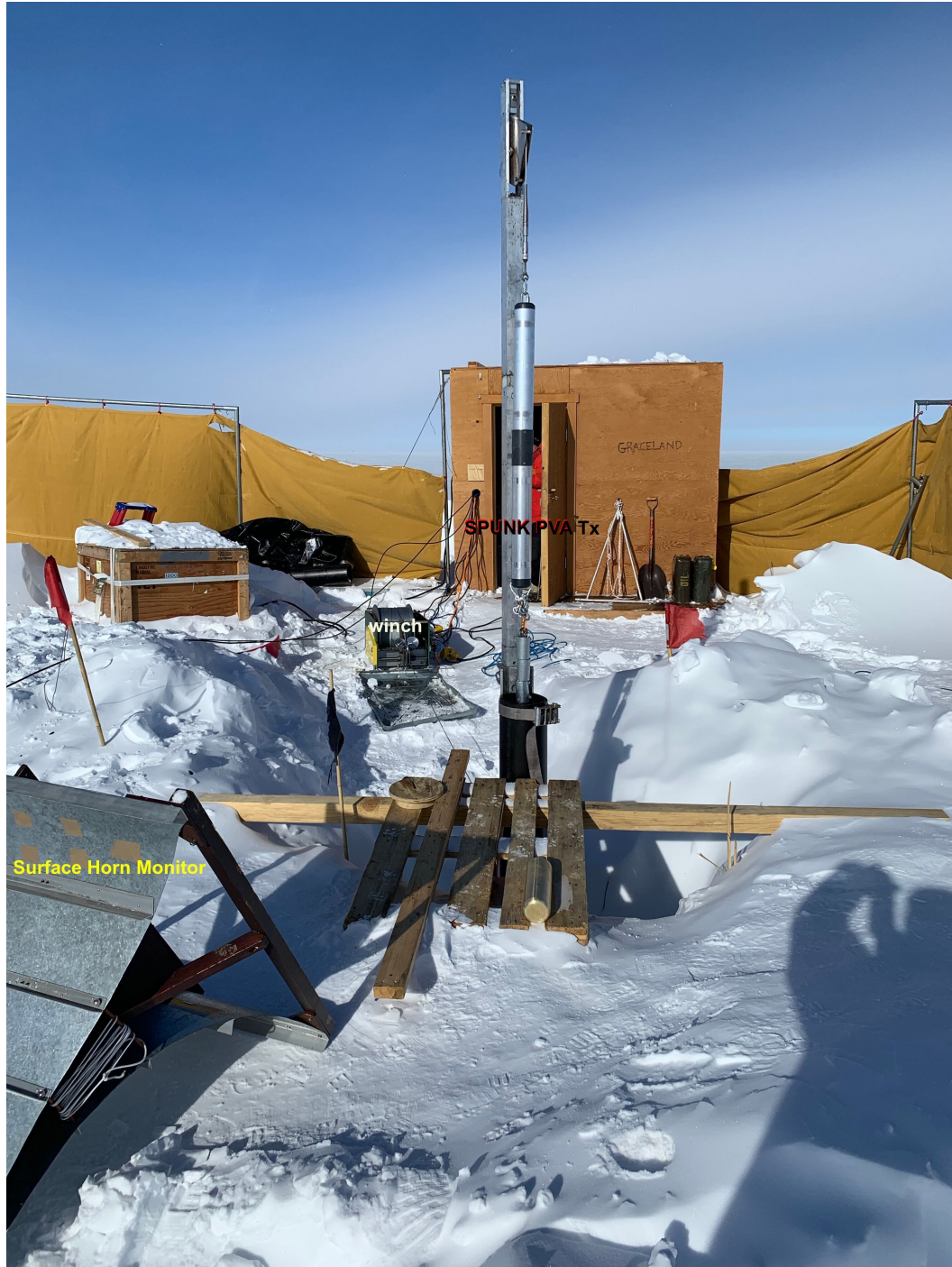
Figure 5. Photograph of experimental set-up prior to lowering transmitter antenna into hole. Visible are vertically-aligned SPUNK PVA (indicated with black label), one of the two surface horn antenna monitors (SurfMon1, as indicated with yellow label) and winch (as indicated with white label). Note weight stack at the bottom of SPUNK PVA to ensure buoyancy after descent into SPICE core hole, slightly obscured by above-surface black cylindrical hole casing.
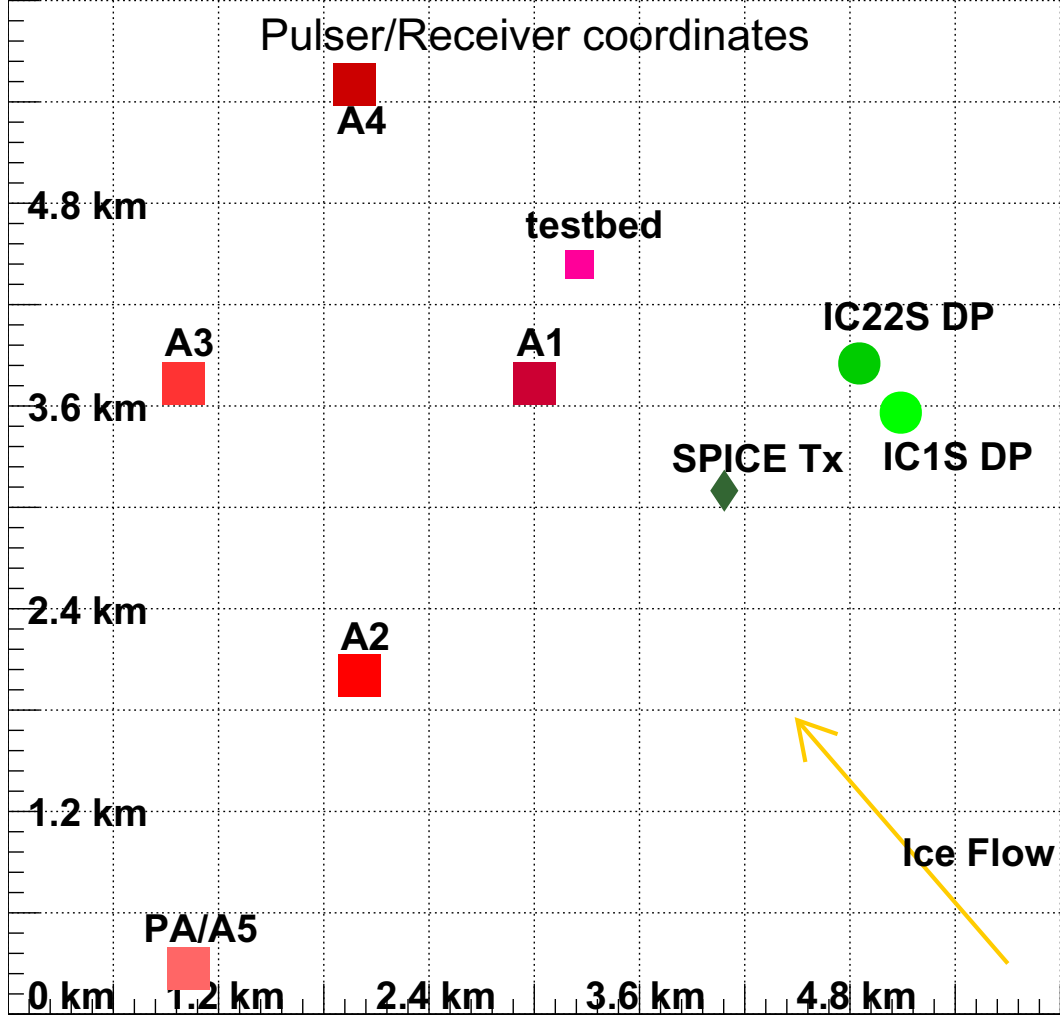
Figure 6. Geometry of ARA receiver stations (red/pink) relative to transmitter sources at IC1S, IC22S and SPICE borehole. Phased Array receiver string is co-located with station A5.

hibited a temperature-dependent pulser period between 3–8 seconds, and also emitted noticeable after-pulses, signals were emitted by the HVSP and IDL pulsers at approximately 1 Hz. Fig. 8 shows the time-interval between successive ARA station triggers during broadcasting. The periods of the two pulsers are evident from Figure 8.

3 Observations and received signal waveforms

Figure 9 shows a waveform display for an event trigger recorded in ARA station A4. In typical events, approximately 1000 ns of data are recorded at a sample rate of 3.2 GSa/sec. In the Figure, the top two rows correspond to the voltage vs. time profiles for the VPol channels; the lower two rows present the voltage vs. time for the HPol channels. Conspicuous in these plots are 'double-pulses', one resulting from the direct trace ('D') from source to receiver, and a second, delayed signal resulting from refraction ('R') through the ice, characteristic of broadcasts from the 'visible' zone, and below the shadow boundary. Within the data acquisition system (DAQ), the channels are ganged according to the icehole ('string') into

– 9 –
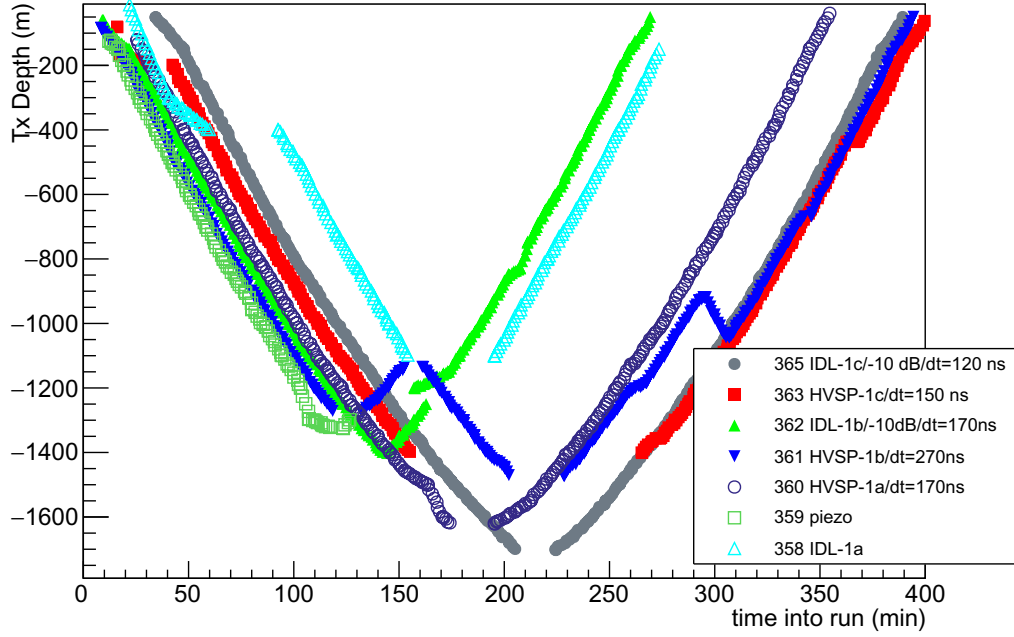
Figure 7. Summary of SPICE core SPUNK PVA drops, conducted from Dec. 23–Dec. 31, 2018. In all cases, t=0 corresponds to start of antenna drop. Also indicated are the Julian day of the run, the pulser used (piezo, IDL or HVSP), the attenuation used on the transmitter output (10 dB for runs on days 365 and 362), and the 3-fold coincidence window used for the ARA receiver stations trigger.

which the antennas are deployed. During the time that these data were taken, the gain on the channels in string 4 was noticeably reduced.

We note considerable signal power in the HPol channels (lower two rows) in Figure 9. The cross-polarization SPUNK PVA signal strength in the lab, in pre-deployment testing, was observed to be reduced by 6 dB in power relative to the co-polarization signal strength, typical of the fat dipole model. For the *in situ* SPICE tests, and assuming the estisol+ice environment does not significantly change the SPUNK PVA beam, the measured HPol:VPol signal strength at the receiver expected for the vertically-oriented SPUNK PVA transmitter should be reduced by the product of that 6 dB transmitter cross-polarization suppression, multiplied by the intrinsic relative HPol:VPol receiver gain ratio over the spectral bandwidth corresponding to the SPUNK PVA output signal. Empirically, we observe unexpectedly large variation in both the HPol, as well as (independently) the VPol signal strength as a function of depth into the SPICE borehole, for both shallow (shadowed) as well as deeper (non-shadowed) geometries, suggestive of multi-path interference effects. Selecting the stations with the most vertical signal incidence angles (A1), intermediate elevation signal incidence angles (A3), and the most horizontal incidence angles (A5), additional empirical features of the measured data are presented in Figures 10–13. Particularly for A3, we observe significant VPol signal enhancement around the depth of the shadowed/non-shadowed transition, as expected for flux focusing around a caustic. The power spectra shown for A1 exhibit an evident shift to lower frequencies (f<500 MHz) as the transmitter emerges from the shadowed regime. Figure 13 shows the A5 station signal-to-noise ratio, as a function of transmitter depth.
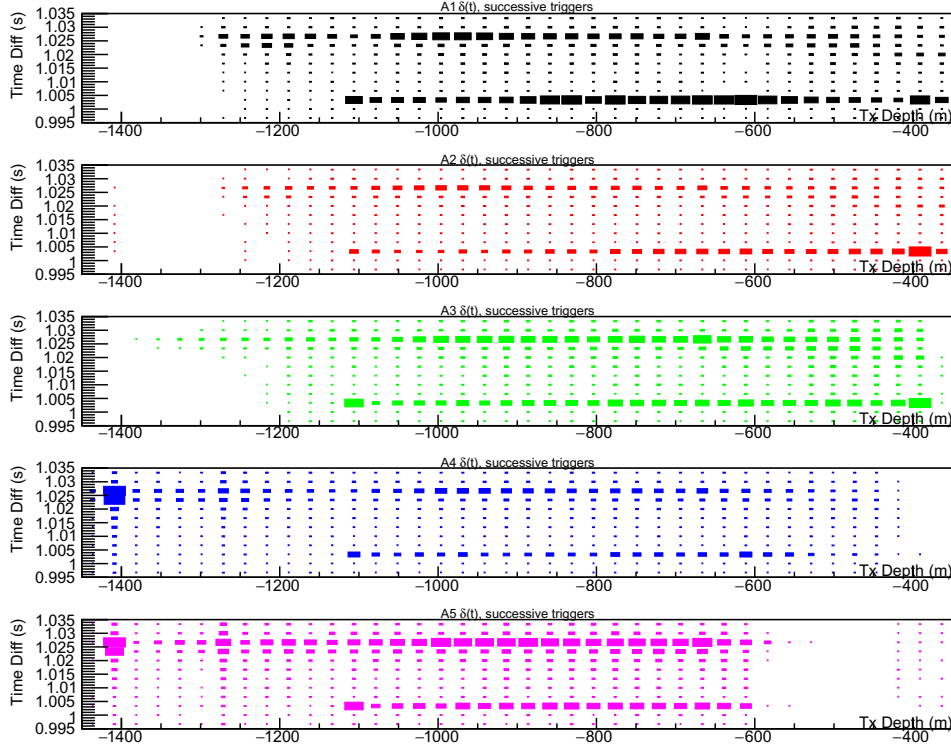
Figure 8. Time difference between successive triggers for ARA receiver stations (vertical axis, in seconds), as function of SPUNK depth (in meters), showing the 1028 ± 0.9 ms period of the HVSP (Julian days 360, 361 and 363) and 1004 ± 0.7 ms period of the IDL (Julian days 358, 362 and 365) PVA transmitters. The A1–A3 trigger performed irregularly for depths greater than approximately 1200 m.

We expect a gradual reduction in observed signal owing to the warmer, more absorptive ice being sampled as the transmitter descends ($1/r$ effects are negligible for this geometry, and have been corrected for in the Figure.). We also observe an apparent modulation of the signal amplitude with depth; similar features have been reported in concurrently-recorded ARIANNA data[32]. Although we cannot rule out the possibility that this is an antenna effect, we note that no such angular-dependence in signal strength was observed in pre-deployment anechoic chamber calibration. Overall, we note considerable deviations from smoothness in these distributions. Although a comprehensive first-principles model for shadow and near-shadow zone propagation has yet to be developed, a successful model should, in principle, reproduce these observations.

4 Hit-Finding and Pattern Recognition

The standard ARA source reconstruction algorithms utilize channel-to-channel waveform cross-correlations to extract relative signal arrival times in the antennas that comprise a single station. Combined with antenna geometry and location information, relative 'hit' times on two vertically-displaced channels (i.e., one hit-time difference) are sufficient to infer a signal arrival direction in elevation, assuming an incident plane wave. As shown in Figure 9, there are doublets of pulses arriving within a typical $\mathcal{O}(1000$ ns) window – the direct D signal arriving from below the centroid of the array, followed by the refracted R pulse arriving from
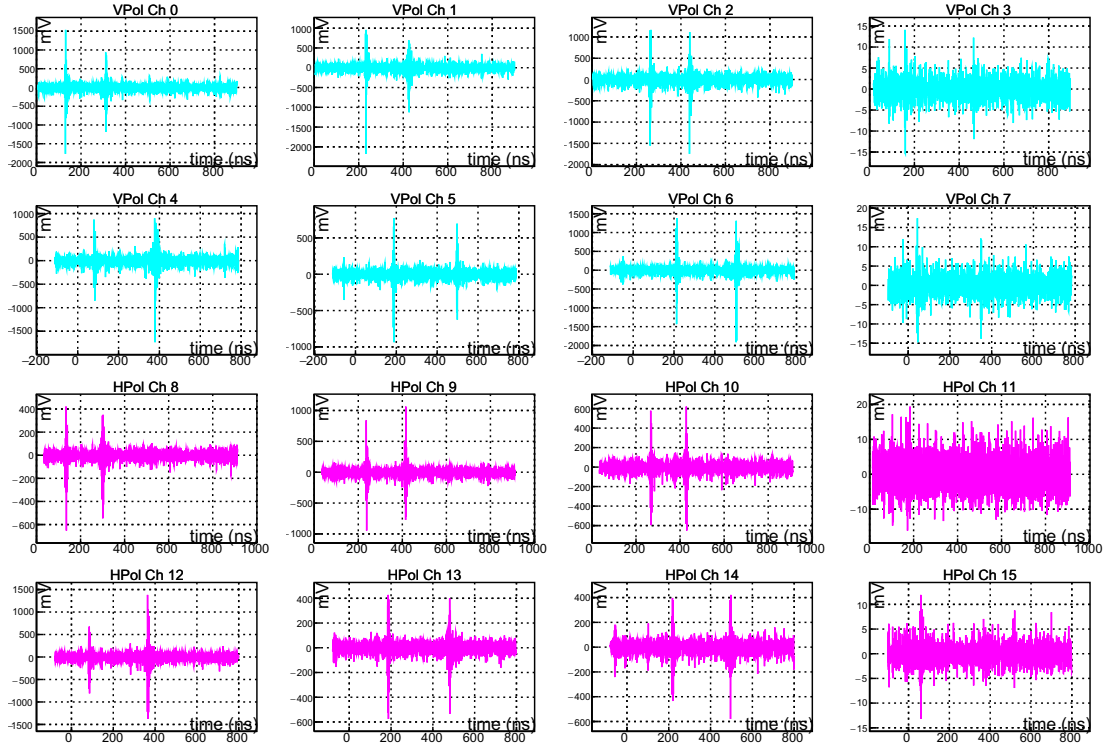
Figure 9. A4 event display (milliVolts [y-] vs. nanoseconds into waveform ([x-]) for four top VPol antennas (top row, cyan), bottom VPol antennas (second row, cyan), top HPol antennas (third row, magenta) and bottom HPol (fourth row, magenta) antennas during SPUNK PVA pulsing. During this data-taking the gain for string 4 (VPol Ch3, VPol Ch7, HPol Ch 11, and HPol Ch 15) was reduced relative to other channels.

above the array centroid. In Figure 14, we show the inferred elevation angle for same-hole channels, by projecting the incident plane wave onto the vertical (z-) axis. As expected, as the transmitter descends into the SPICE core icehole, the D and R incidence angles deviate approximately symmetrically from 90°. Figure 15 displays the corresponding data derived from the Phased Array[33], deployed at the location of A5, and consisting of a single string of multiple VPol antennas, qualitatively consistent with the features of Fig. 14.

4.1 Direct and Refracted Double Pulses

For fixed receiver depth, the time difference between the Direct and Refracted pulses is expected to increase roughly linearly with source depth once the transmitter emerges from the 'shadowed' to the 'visible' region, qualitatively consistent with the trend observed in our data (Figures 15 and 16). Extrapolating the x-intercept of the (D,R) time differences allows us to infer the boundary between the shadowed vs. unshadowed regions, for a given receiver array. The z-value corresponding to the depth of the 'edge' of the shadow region for all of the channels for which we have 'good' ARA station data is presented in Figure 17. Presented errors are estimated by considering the variation in x-intercept using different parameterizations for the refractive index profile. As indicated in the Figures above, there is often measurable signal from the SPUNK PVA while the PVA is still in the nominal 'shadow' regime, corresponding to the upper few hundred meters of the ice sheet. Measurable signals emanating from within the nominal shadow zone at both the South Pole and Moore's Bay have
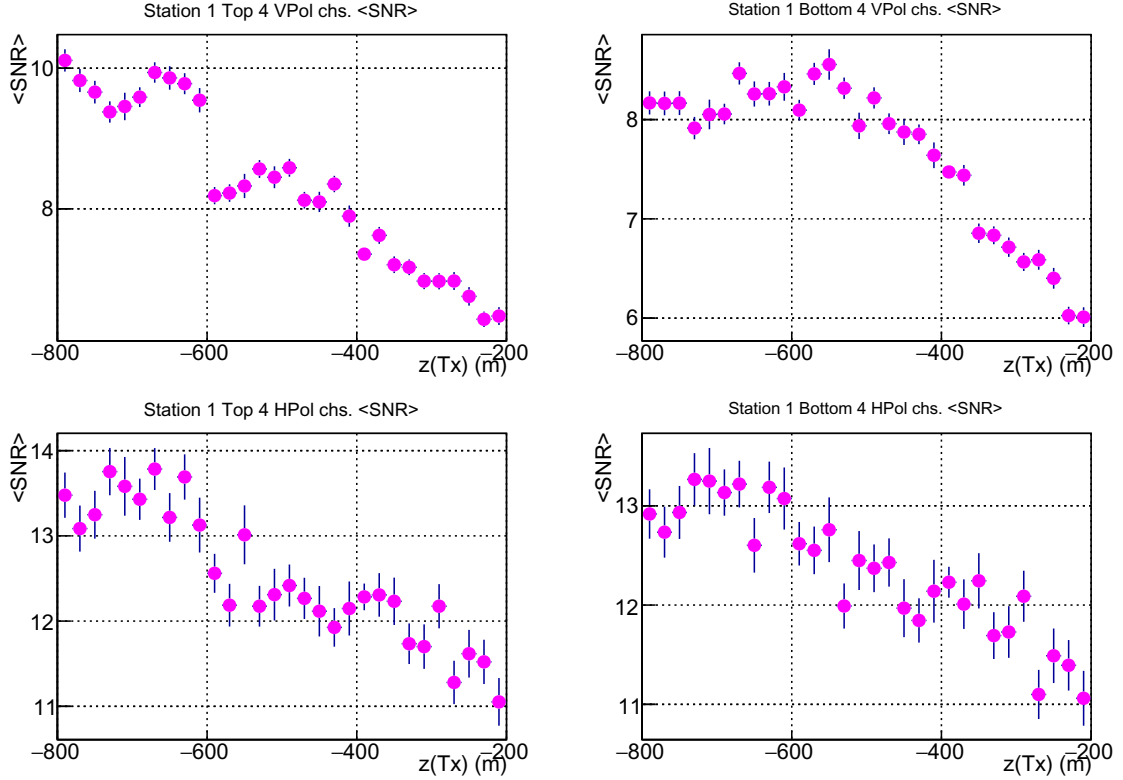
Figure 10. A1 Signal-to-Noise ratio, as function of transmitter depth. Note the enhancement in VPol SNR as the transmitter crosses the shadow zone boundary at approximately z=-600 m.

been previously reported elsewhere[22] and may result in enhanced aperture for radio-based neutrino detectors.

4.1.1   Implications for refractive index profile

Note that, although the vertical separation between the four shallower VPol antennas relative to the four deeper VPol antennas is only 20 meters, the (D,R) time difference separations for the two sets of antennas (shallower vs. deeper) are markedly different, suggesting that the $\delta_t(D, R)$ data might be used to extract the true n(z) profile from a global fit. In principle, of course, if one has absolute timing relative to the signal emission time, the absolute transit time from transmitter to receiver, which depends on the integrated travel time through a region of varying refractive index, might be used to extract n(z). That measurement, however, is susceptible to combined systematic uncertainties in the geometry of the array laterally, as well as vertically. The time differences between the measured D and R signal arrivals circumvent those uncertainties. The constraints in our fits are the measured $\delta_t(D, R)$ time differences as well as the extrapolated depth of the shadow/non-shadow transition. Quantitatively, the gradient in $\delta_t(D, R)[z_{Rx}]$ is of order 3–4 ns per meter in receiver depth, compared to the canonical 1 ns timing uncertainty in the ARA data.

The current preferred ARA simulation (AraSim) model parameterizes the refractive index dependence on depth using the exponential form n(z)=1.78+Bexp(Cz), as expected for the density profile $\rho(z)$ of a fluid under its own gravitational stress, with B=0.43 and C=0.0132 and depth negative [meters]. However, the existing South Pole density data sug-
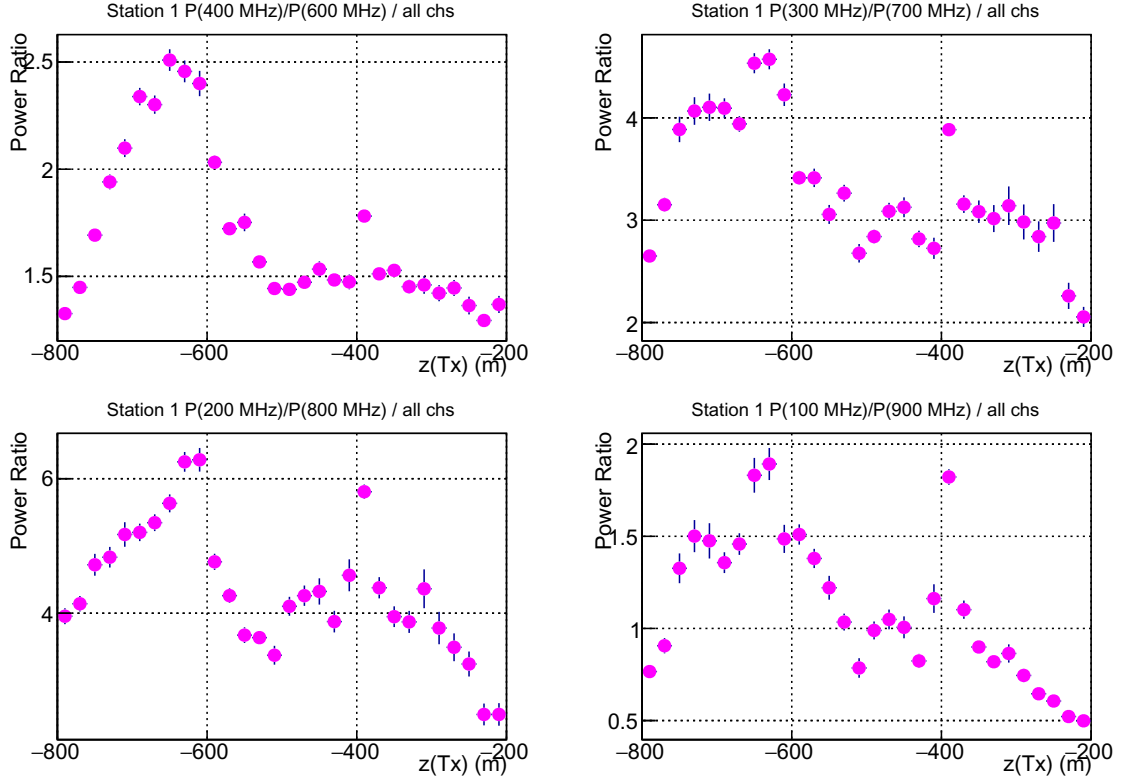
Figure 11. A1 ratio of VPol Signal Power in indicated frequency bands, as function of Tx depth. Top left panel, e.g., displays total signal power in 350 MHz – 450 MHz band relative to 550 MHz – 650 MHz band.

gest non-monotonic behavior in the upper 20 meters, as also indicated by older RICE experimental measurements (e.g., Figure 3 of [22], and also suggested by the observation of signals originating from 'shadow'ed ice volumes at South Pole[22]). A sigmoid functional form allows a 'flattening' of the refractive index in the depth interval indicated by the RICE data, and asymptotes to the ARA functional form at depths below z=-25 meters. We initially determine the best-fit sigmoid functional parameters using the $\delta_t(D, R)$ data from station A2. For A2, signals refract and 'turn over' at a maximum depth of 25 meters within the snow surface, for all SPICE geometries. A comparison of the functional form extracted from the fit to the A2 data with existing density data (extrapolated to n(z) using the phenomenological ansatz that the refractive index is a linear function of density n(z)=1.+0.86$\rho(z)$)), and also the current ARA model is presented in Figure 18.

We have compared the sigmoid vs. exponential-form $\delta_t(D, R)$ predictions for double-pulses observed using the deep pulsers IC1S and IC22S. For the deeper stations A3–A5 as well as the IC1S and IC22S pulsers, our sigmoid model results in either equivalent, or improved chi-squared values relative to the Arasim exponential. However, for station A1, for which rays refract to the receivers at shallow SPUNK depths, or reflect for deeper source locations, Arasim is favored, suggesting the possibility that the ice may not be as uniform over the multi-km scale as initially assumed. As an alternative, a modified exponential functional form using B=0.61 and C=0.0172 gives superior results compared to both the default AraSim n(z) profile as well as a sigmoid for the majority of the data-sets used for calibration,
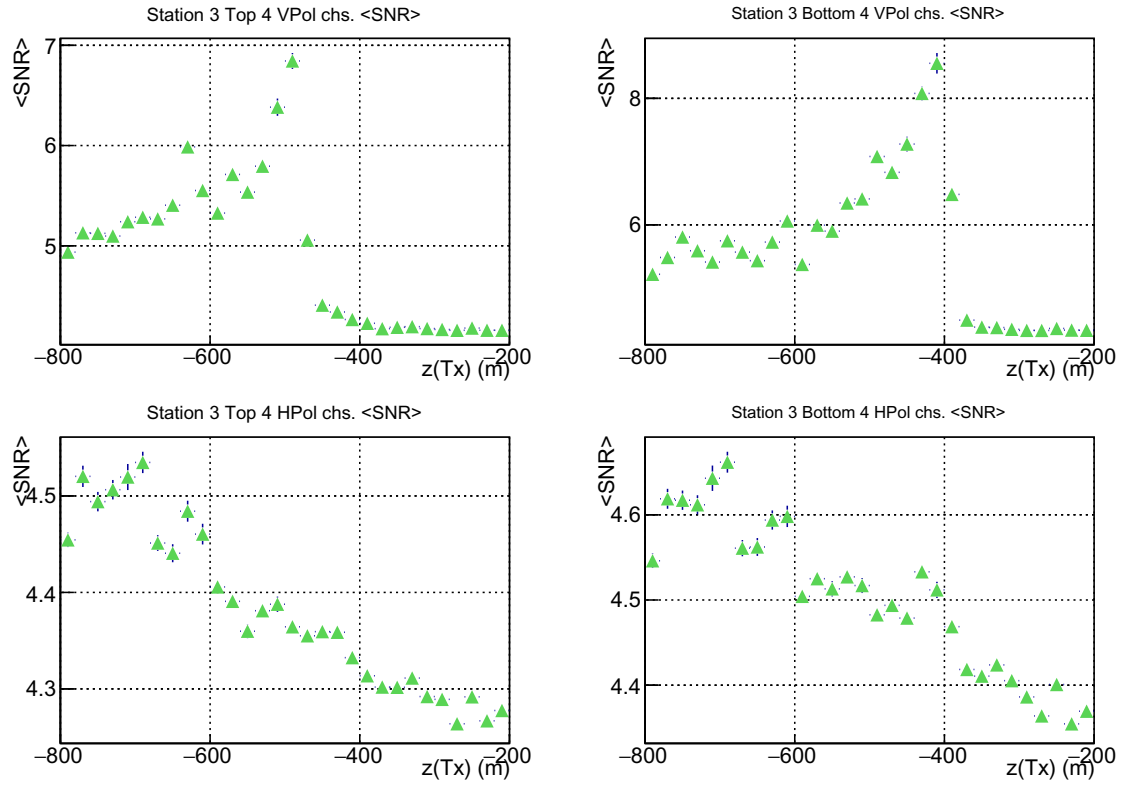
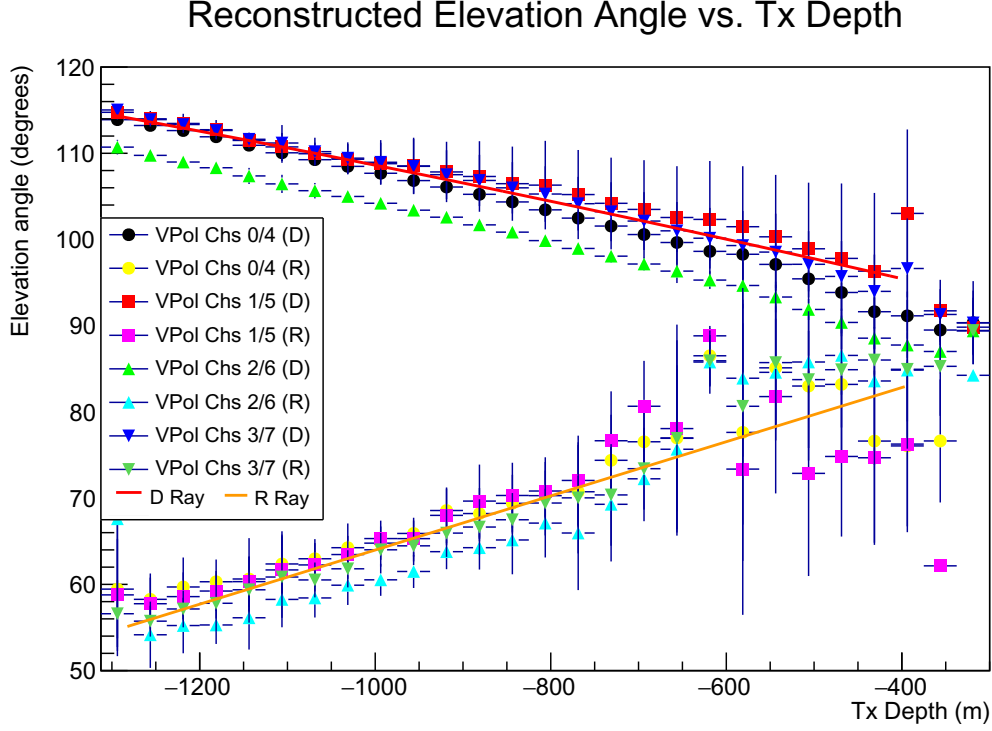**Figure 12**. A3 Signal-to-Noise ratio, as function of transmitter depth.
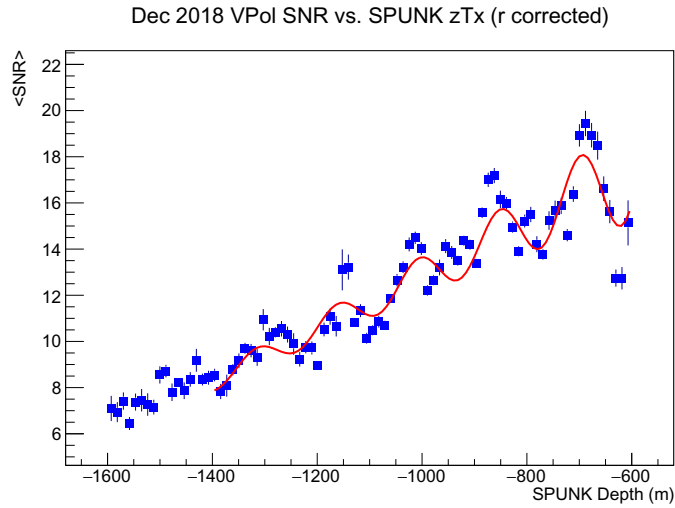
Figure 13. VPol Station A5 measured Signal-to-Noise ratio as a function of depth. The SNR data have been fit to a functional form $A(z) = A_0 \cos(kz + \phi_0)$.

Figure 14. A2 reconstructed (points) incident elevation angles for Direct and Refracted rays, as a function of depth of SPUNK PVA. Overlaid curve shows expectations from ray tracing. Note that at shallow depths, the decreasing time difference, and therefore increasing overlap between the D and R rays impedes separating the two signals in a given waveform.

although it does not incorporate the measured 'break' in the South Polar refractive index at shallow depths and underestimates the implied surface ice density. Figure 19 shows the goodness-of-fit comparison of the default ARA refractive index model ("AraSim") compared to a revised exponential model, with B=0.61 and C=0.0172, as well as the sigmoid model discussed previously. Our revised exponential model, overall, gives the best match to observation, although it also results in an underestimate of the ice density at the surface. In practice, the different parameterizations lead to very similar neutrino sensitivities. As measured by the so-called 'effective volume' ("V_{eff}", or the equivalent volume of ice over which neutrino interactions are measurable), the tested refractive index parameterizations give V_{eff} estimates that agree to within 3% of each other.

5   Birefringence Measurements

At radio frequencies, the bulk birefringence of polar ice arises due to the combined effect of the ice fabric (the orientation distribution of ice crystals) and the stretching of individual ice crystals. Whilst individual ice crystals have uniaxial symmetry, in the general case, polar ice is a biaxial medium (three different principal indices of refraction, which are aligned with the principal axes of the fabric orientation tensor). Given the two in-ice strains which break 3-space symmetry (vertical compression and horizontal ice flow), a reasonable ansatz aligns one principal axis in the direction of local ice flow ($\hat{e}_1$), one axis vertical ($\hat{e}_3$) and a
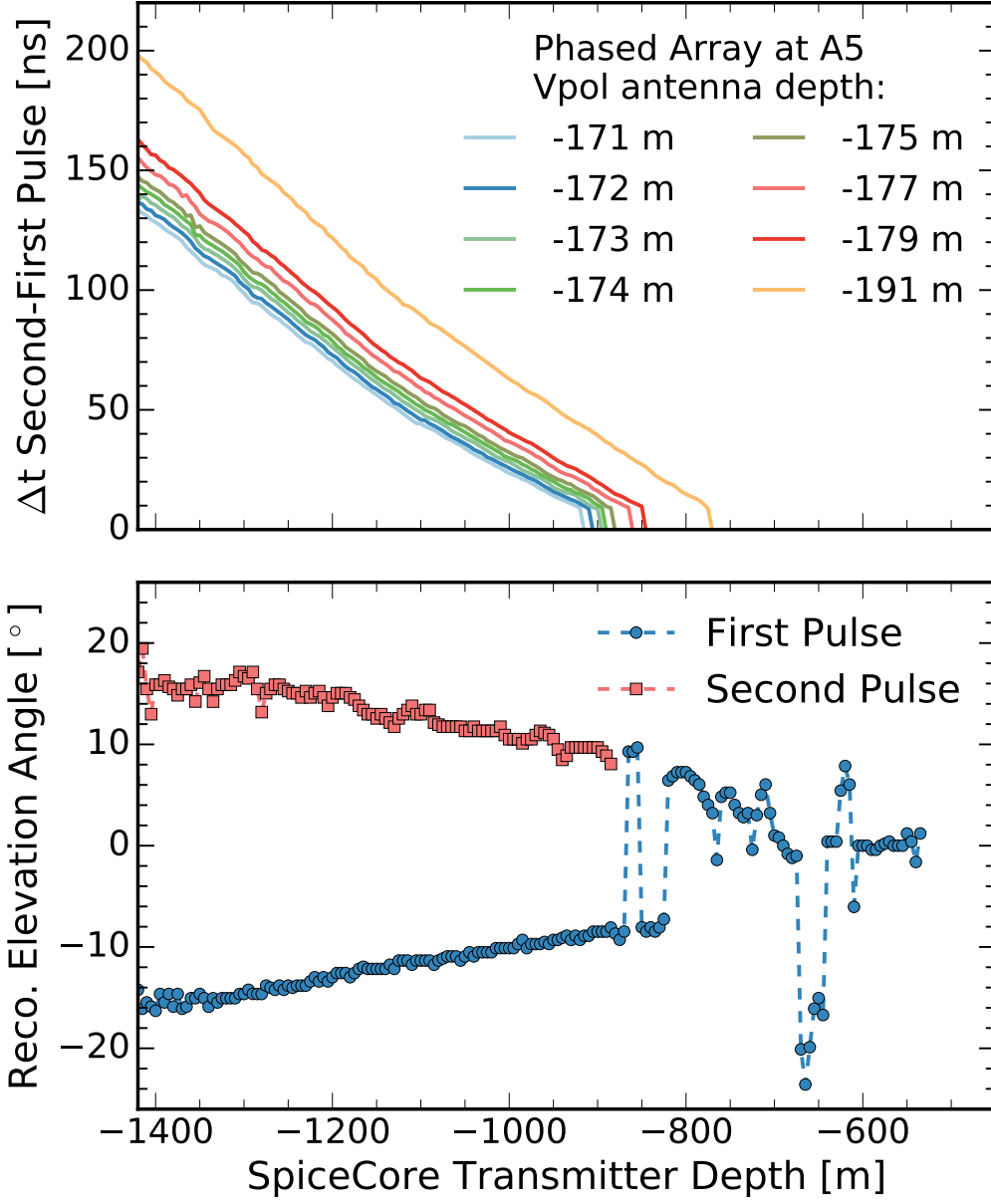
Figure 15. (D,R) time difference (top) and also elevation reconstruction (bottom) for Phased Array.
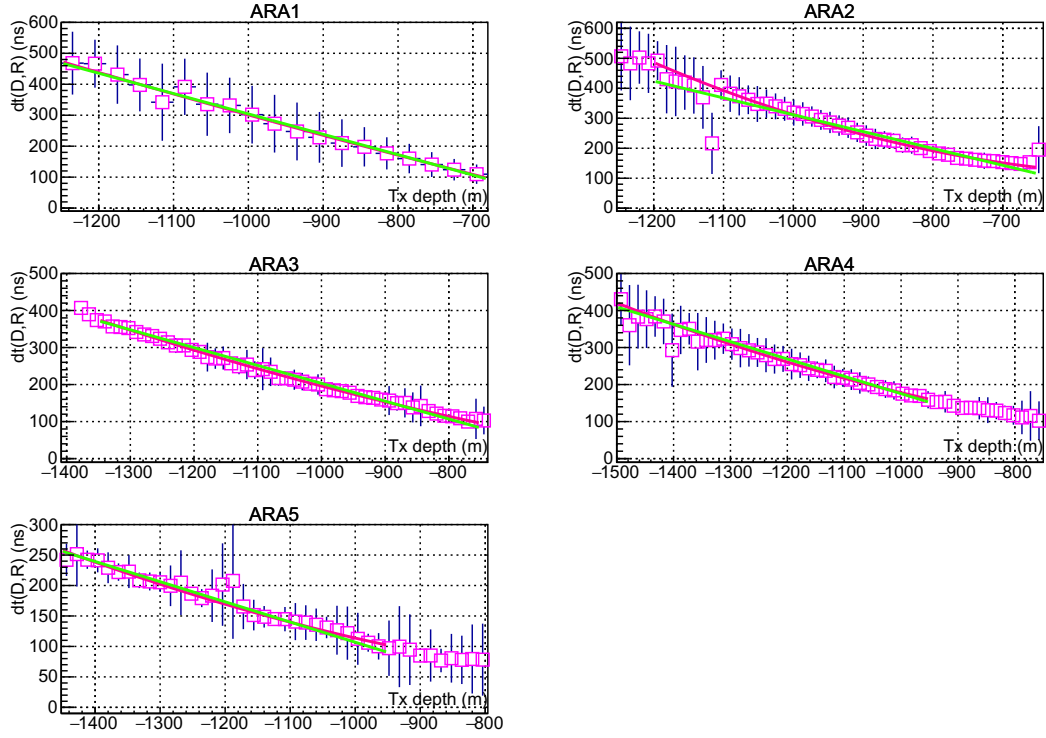
Figure 16. Time differences (vertical axis, in units of ns) between Refracted (R) and Direct (D) pulses as a function of PVA depth into SPICE core (horizontal axis, in units of meters). Apparent 'flattening' of curves for small time difference values is an artifact of limitations of the double-pulse hit-finding algorithm.
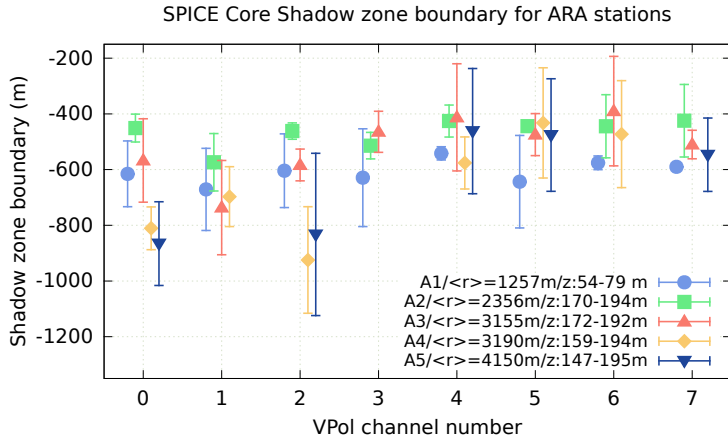
Figure 17. Derived value of depth of shadow/visible zone boundary for VPol channels of ARA stations A1-A5, obtained by extrapolating $\delta_t(D, R)$ curves to zero time difference. Average radial separation from station to SPICE core, and depth of VPol receivers (with channels 0-3 shallowest and channels 4-7 approximately 20-30 m deeper) are indicated in legend. Error bars indicate estimated uncertainties in shadow zone boundary extrapolation.
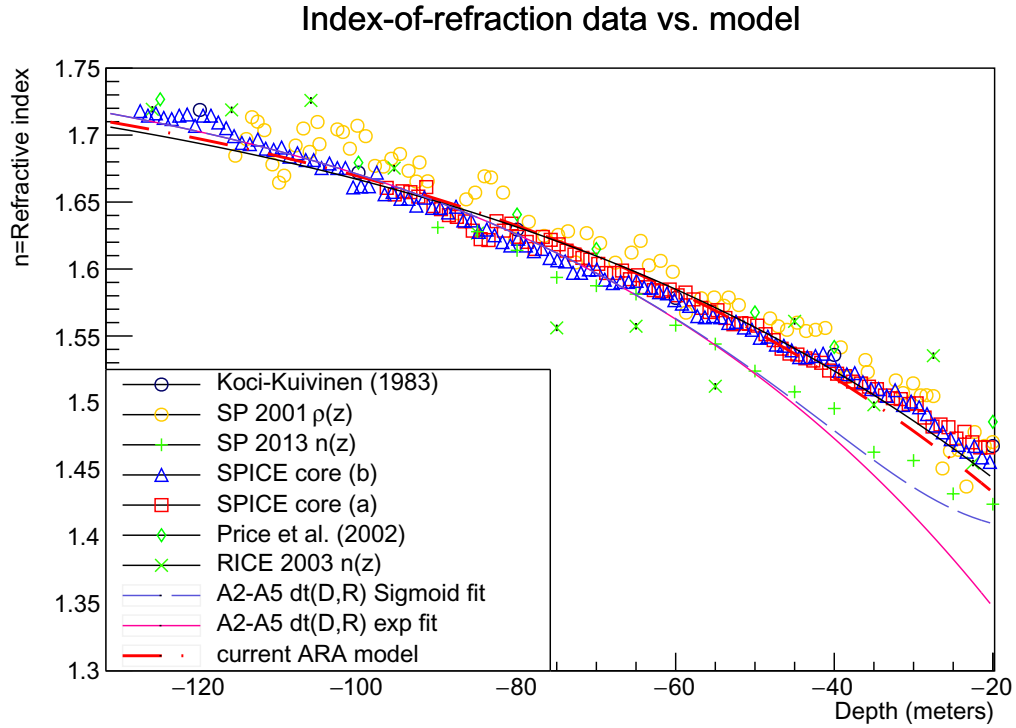
Figure 18. Comparison of current ARA model (red, dashed), as well as sigmoid functional fit to ARA $\delta_t(D, R)$ data with existing South Polar density and refractive index data. Density data are drawn from Koci-Kuivinen[34], measurements based on a 2001 South Pole core[35], Price *et al.*[36], and density measurements from the recent SPICE coring efforts (provided by Murat Aydin, private communication).
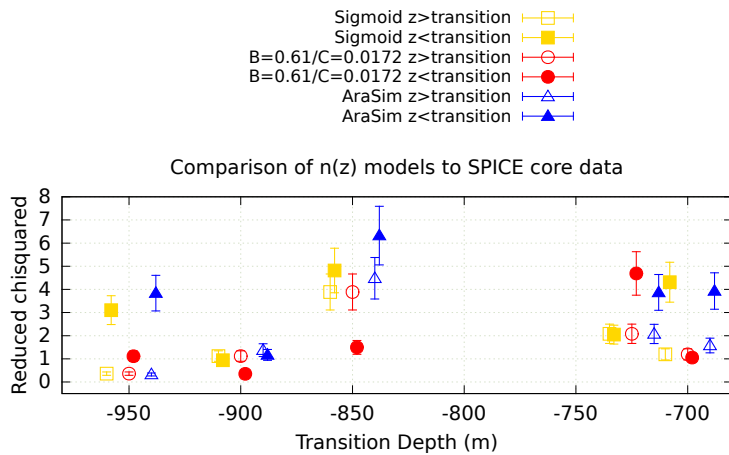

Figure 19. Results of fitting three models for refractive index profile to SPICE core data. For these fits, we present results separately for the two indicated depth intervals.

third axis $\hat{e}_2$ perpendicular to both $\hat{e}_1$ and $\hat{e}_1$, as outlined previously. An electric field vector polarized along some arbitrary direction at the source is then projected into the three orthogonal planes defined by these three axes (e_1e_2, e_1e_3 and e_2e_3); the amplitude within each plane is uniquely determined by the condition that the Electric field be transverse to the Poynting vector ($\vec{E} \times \vec{B} = \vec{S}$). In this description of birefringence, each of the three allowed oscillation directions of the Electric-field components, separately confined to an orthogonal plane, then projects onto the axes defining that plane; those separately projected components subsequently propagate with the wavespeed specific to that polarization component. I.e., the E-field vector confined to the e_1e_3 plane is then resolved along the e_1 and e_3 axes; each of those polarization components propagate with velocity c/n_1 and c/n_3, respectively, with c=0.2998 m/ns. Note that transversality is not retained for these final, projected components, although the 'parent' electric field polarization, confined to one of the allowed e_ie_j planes, is perpendicular to both $\vec{B}$ and $\vec{S}$. Formally, the propagation-vector $\hat{k}$, the Electric Displacement field $\vec{D}$ and the Magnetic Intensity $\vec{H}$ comprise a right-hand coordinate system: $\hat{D} \times \hat{H} = \hat{k}$. Similarly, the direction of the Poynting Vector $\vec{S}$ is given by $\hat{E} \times \hat{H} = \hat{S}$. For a birefringent medium, however, $\hat{D}$ is, in general, offset from $\hat{E}$ by some angle θ, so that the signal propagation direction $\vec{k}$ is offset from the energy flow direction $\hat{S}$ by the same angle θ (again violating transversality). The Poynting vector is therefore a 'composite' of energy transport along both the ordinary and extraordinary axes.

The RICE[14, 37], ANITA[10], and ARA[13] experiments have all made extensive measurements of the polarization dependence of radio-frequency signal amplitudes propagating through cold polar ice. The first RICE measurements were limited to signals broadcast vertically into the ice from the surface and reflecting off internal conducting layers (typically, ash resulting from volcanic eruptions)[14]. Waveforms were recorded as a function of the orientation of the polarization axis, taken at roughly 30-degree azimuthal increments in the horizontal plane, relative to the local ice flow direction. Those first measurements indicated uniformity of echo return times for all measured polarizations, to a depth of approximately 1.5 km into the ice sheet, at variance with volumetric scattering measurements made at Dome Fuji[38]. A second set of measurements were made for RF signals propagating vertically through the entire 2.8 km thick ice sheet, and observed approximately 30 microseconds later, after reflecting off the bedrock. Data from those studies demonstrated a maximal/minimal wavespeed for polarizations aligned parallel/perpendicular to the local ice flow direction, with an asymmetry (i.e., time-difference divided by total transit time) of order 0.15% between the two extrema[14]. These results were somewhat at variance with simple expectations – in the lower-half of the ice sheet, the COF should be dominated by a uniaxial, vertical alignment, with no expected contribution to birefringence.

Our initial ARA time-difference asymmetry study for horizontally propagating signals[13] used 2015 data collected using the IC1S and IC22S radio transmitters. Since those data were collected, ARA station A4 was commissioned and analysis techniques improved. Broadcasts from a transmitter in either the SPICE core hole, or the IceCube deep pulsers IC1S and IC22S, propagate RF at directions roughly parallel relative to the local ice flow direction to A4, and therefore allow a direct comparison of the asymmetry in the arrival time-differences between horizontally vs. vertically polarized signals, for which receiver systematics (such as angle-of-incidence corrections) should largely cancel. Figures 20 and 21 show the HPol-VPol time-difference asymmetries measured for broadcasts from the SPICE core icehole and the deep pulsers, respectively. In both cases, although we observe a time-difference asymmetry for station A2, we observe no obvious asymmetry for station A4 (propagation parallel to local

ice flow direction). These conclusions are consistent with observations of SPICE signals
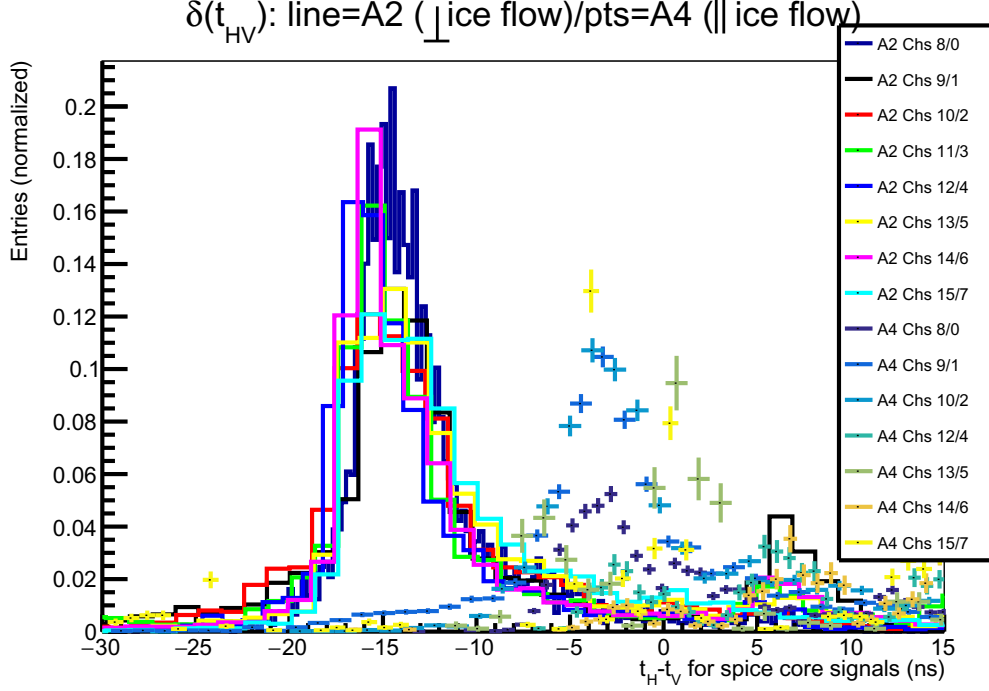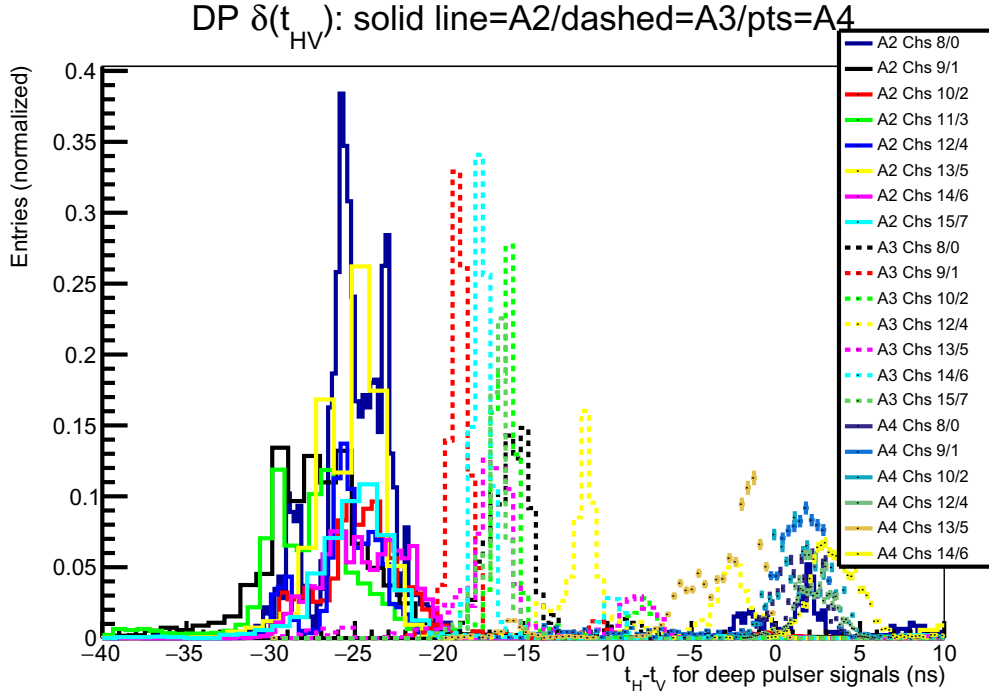

Figure 20. Summary of birefringence measurements (transmitter=Spice Core pulser), comparing data from stations parallel vs. perpendicular to ice flow. We note that a) the resolution in the HPol-VPol time asymmetry is approximately 2-3 ns for most channels, and b) there are very few conspicuous 'outliers'.

propagating to ARA station A1 (Fig. 22), also aligned parallel to the local ice flow direction, albeit at approximately 40% of the horizontal displacement relative to the source, compared to station A4. Interestingly, A1 data indicate an overall positive shift of HPol relative to VPol. ARA Station A5, like Station A2, is approximately perpendicular to the ice flow direction, however, owing to the large separation distance, the small signals observed on the HPol channels (for both SPUNK or Deep Pulser pulsing) disallow a reliable birefringence extraction.

We note that similar measurements for the ARA testbed, using the deep pulsers IC1S, IC22S, and IC1D, yield (H-V) preliminary time differences of -9.1, -9.1 and -7.8 ns respectively, although systematic errors have not been assessed. For those testbed measurements, the arrival times of the testbed VPol channels (3,6,2 and 4) were added and compared to the summed arrival times of the testbed HPol channels (0,1,5 and 7). Each of the four testbed strings has one VPol and one HPol channel, separated by 5 meters vertically, with HPol on top in two strings and VPol on top in the remaining two strings. A simple comparison of the sum of the VPol times vs. HPol times therefore directly gives the birefringent asymmetry, independent of arrival angle corrections. The testbed was de-commissioned in December, 2016, and was therefore not active during the December, 2018 SPICE campaign.

To ensure that the observed offset from zero for A2 is not an artifact of a global mis-calibration of relative (H,V) channel delays, we have performed a similar relative-timing analysis using data collected from a surface pulser in both 2015 and 2018. For 2015 surface

Figure 21. Summary of birefringence measurements (transmitter=deep pulsers), comparing data from stations parallel vs. perpendicular to ice flow. We note that all stations are approximately equidistant from the source, and vary primarily in their orientation relative to the local ice flow direction.
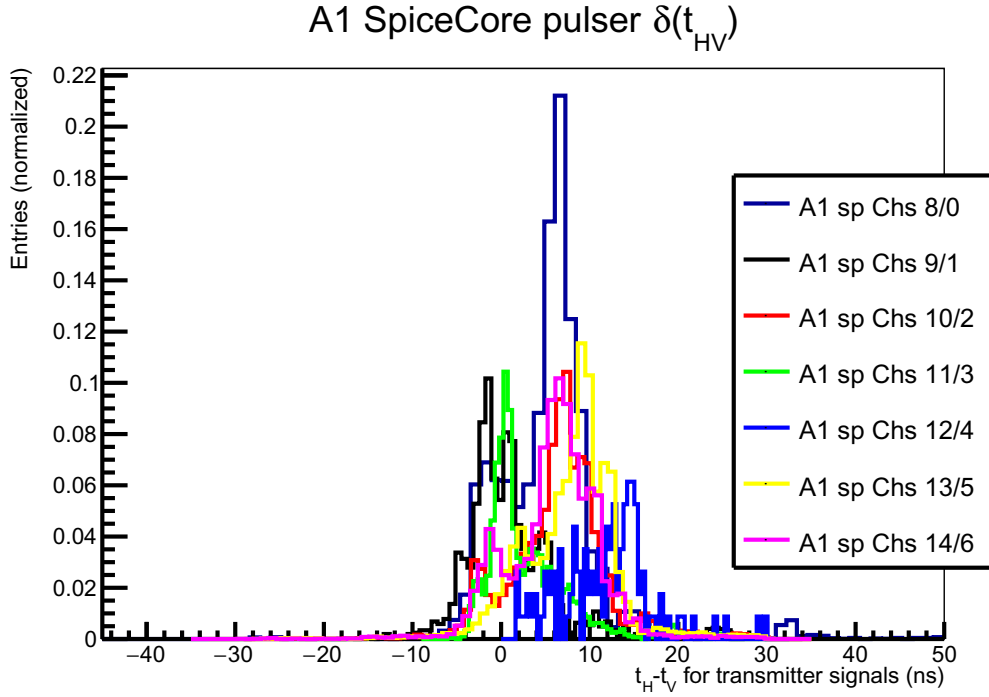

Figure 22. Summary of birefringence measurements (transmitter=SPUNK pulser only) for ARA Station A1.

pulser broadcasts, we observe H/V timing offsets of -10.3 ± 3.6 (A1), -10.9 ± 5.4 (A2), and -13.1 ± 5.4 ns (A3). For 2018 broadcasts, the comparable values for A1, A2 and A4 are -12.3 ± 4.1, -12.2 ± 8.6 and -5.6 ± 17.6 ns, respectively. We note that, for signals arriving at the critical elevation angle of $\approx 35°$, the typical H/V vertical pair separation of 2.5 meters translates to an expected time difference of approximately -10.3 ns, consistent with observations.

5.1 Interpretation

We note the following: a) the ratio of birefringent asymmetries for A2 Deep Pulser pulsing vs. SPICE pulsing is approximately proportional to the pathlength difference for signals arriving from these two respective sources, b) although our A2 data was limited to the 'visible' source range of 600-1100 meter depths, sub-dividing our data into $z < -800$ m vs. $z > -800$ m depth gives the same birefringent asymmetry, on average, to within one ns, consistent with a model where the ice core fabric does not vary significantly over this depth range. The observed nearly linear variation of asymmetry with range suggests a linear parameterization of this dependence, which might then be used to translate a measured birefringent asymmetry from an unknown neutrino interaction point in-ice to estimate the range to interaction point (necessary for an estimate of the neutrino energy). Such a linear fit is shown in Figure 23.
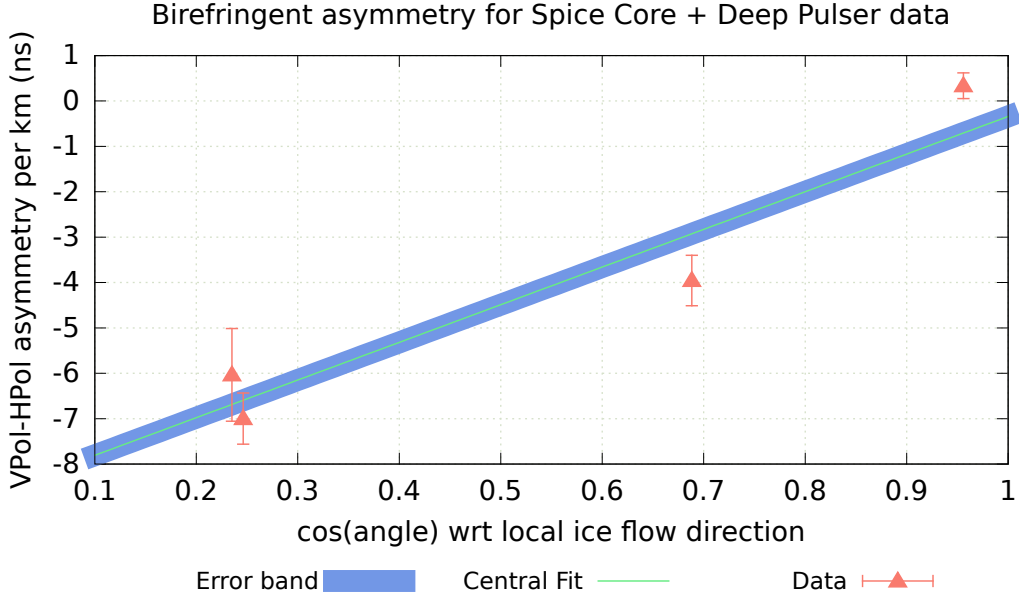
Figure 23. Linear fit of measured birefringence asymmetry (per km), as function of signal propagation angle relative to local ice flow direction (determined experimentally from interferometry). We fit our birefringence time-difference measurements to the functional form $\delta_t(H-V)[\text{ns/km}] = a\cos\theta + b$, with θ the opening angle in the horizontal plane between the signal propagation direction and the local ice flow direction, and find a=8.3±1.3, and b=-8.6±0.9 (errors combined statistical and systematic).

6 Radio-frequency attenuation length (L_{atten}) measurements

Measurements of the absorptive component of the dielectric constant ϵ'' require baselines comparable to several e-foldings of the signal amplitude to avoid being dominated by sys-

tematic uncertainties – in the radio-frequency regime, the ice attenuation length is expected to increase by a factor of $\sim$5 over the temperature range $0 \rightarrow -55$ C, corresponding to the temperature variation between the bottom and the top of the ice sheet at the South Pole[36], and consistent with the overall trend observed in Fig. 13. Logistical considerations favor bi-static radar measurements, in which RF from a surface transmitter is reflected off the bedrock and then measured in a nearly co-located surface receiver ("bottom bounce"). The multi-kilometer, through-ice path, over a baseline d_{ice} is then compared with a through-air path d_{air}. In that case, assuming 3-dimensional flux spreading and attributing all losses beyond the expected $1/r$ diminution of signal amplitude with distance to ice signal absorption, the antenna gain cancels in comparing the through-air with the through-ice signals and the attenuation length L_{atten} can be extracted from the receiver signal voltages measured over a short baseline in air (V_0) vs. the signal voltage measured over a longer baseline in ice (V_1) via: $V_1/V_0 = (d_{air}/d_{ice})exp(-(|d_{ice} - d_{air}|)/L_{atten}) \times \mathcal{R} \times FFF$, with $\mathcal{R}$ the unknown bedrock RF reflectivity (in the most conservative case, set to 1.0) and FFF the Flux-Focusing-Factor, due to the variable refractive index profile with depth. For the typical bi-static geometry, with nearly vertical propagation from/to the surface, the small-angle approximation gives $n_s\theta_s \sim n_i\theta_i$, with n_s the index-of-refraction of the antenna environment at the surface (presumably, roughly halfway between air and surface snow/ice) and n_i the asymptotic index-of-refraction below the firn; $n_i \approx 1.78$. In that limit, provided the firn layer is a relatively small fraction of the entire ice thickness, $FFF \approx n_i^2/n_s^2$. In addition to systematic uncertainties due to flux-focusing and the bedrock reflectivity, these bottom bounce measurements measure the average attenuation over the entire thickness of the ice sheet, so the L_{atten} dependence on depth must be corrected for. Previous estimates of the depth-dependent attenuation from bistatic measurements were therefore based on unfolding the depth-dependent attenuation length profile from the depth-averaged measurement, combining laboratory measurements of $L_{atten}(temperature)$ with the measured temperature vs. depth profile at South Pole[36]. The depth-averaged measurements are strongly dependent on the inferred ice temperature near the (relatively warm) bedrock, which produces the greatest ice absorption, and therefore dominates the unfolding.

Our broadcasts over long horizontal baselines permit an independent estimate of the radio-frequency attenuation in the upper (colder) half of the Antarctic ice sheet, corresponding to the bulk of the proposed neutrino target volume for experiments based on detection of coherent Askaryan radiation. Both the SPICE core and the IceCube deep RF pulsers allow a more direct determination of L_{atten} using relative signal amplitudes observed at two stations (V_1 and V_2), and also knowing the pathlength from source to receiver (d_1 and d_2, as shown in Table 1), via $V_1/V_2 = (d_2/d_1)exp((d_2 - d_1)/L_{atten})$; this extraction is therefore insensitive to uncertainties in either the bedrock reflectivity or flux focusing. Broadcasts along the horizontal trajectories more typical of neutrino signal geometries are also more sensitive to the possible 'channeling' effects of internal layers than bistatic vertical broadcasts, for which the internal reflection/transmission coefficients are minimal/maximal.

Since the signal from the IC1S and IC22S transmitters is observed to saturate the A1, A2, and A3 receivers, measurements using those deep pulsers were restricted to ARA stations A4 and A5, which were equipped with attenuators at the input to the DAQ so that reliable relative voltage values V_1 and V_2 could be extracted. The ARA Front End (ARAFE) modules used on stations A4 and A5 allow the user to vary the signal attenuation at the ARA antenna output/DAQ input from zero to 12 dB, to mitigate saturation. We make multiple estimates of the VPol attenuation length, by comparing 'same-antennas' A4 top-VPol channel 0 (TV0)

**RF Field Attenuation Length (A4/A5 DP data): <L>=1.43+/-0.25 km**
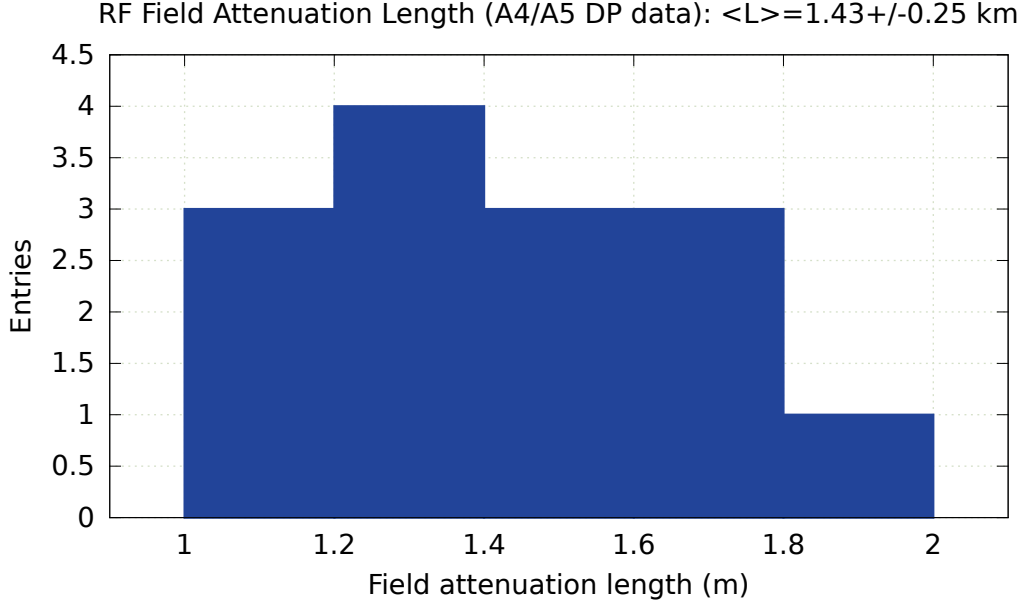
Figure 24. Attenuation length based on relative VPol signal strengths observed in A5 relative to A4 using IceCube deep pulsers IC1S and IC22S as transmitters. To avoid saturation of A4 waveforms, signal gain on A4 was attenuated by 12 dB (later corrected for in off-line analysis) for these runs.

to A5 TV0, etc. Although 16 such combinations (8 VPol channels per receiver station × two deep pulsers; the weakness of HPol signals prohibits an analogous HPol measurement) are, in principle, possible, two combinations were excluded owing to non-functioning channels. The resulting distribution of calculated attenuation lengths is shown in Figure 24; this result is numerically consistent with ∼1.5 km previous estimates for L_{atten} in the upper half of the ice sheet[39].

For the non-saturating SPICE core data, we have taken a more general approach and produce an attenuation length distribution for all possible 'same-antenna' VPol pairs, for any two stations separated by at least two km. We note that this distribution is heavily weighted by station A5, which is furthest from the SPICE core. We additionally separate our measurements by day, in order to probe possible differences in transmitter systematics. We note that the data from Day 358, for which a piezo-based signal generator was employed, shows a somewhat longer attenuation length distribution than for the other three days. We regard those data as most prone to systematic uncertainties than for the other days on which data were accumulated, owing to the significantly less sharp signals, as well as the possibility of multiple after-pulses in a typical piezo-signal waveform capture. Despite those uncertainties, the piezo data again indicate long attenuation lengths.

If the amplitude resolution were infinite, each measurement would yield identical estimates for the attenuation length. Although local calibration pulser events show clear fluctuations in the observed channel-to-channel signal amplitude, Monte Carlo simulations indicate that the effect of finite resolution is to introduce some width to the derived L_{atten} distribution, but not to significantly shift the peak value of that distribution. We correspondingly interpret the peak value of our L_{atten} histograms as the radio-frequency electric field attenuation length, averaged over the upper 200-1200 m of the South Polar ice sheet. Our measurements (Figure
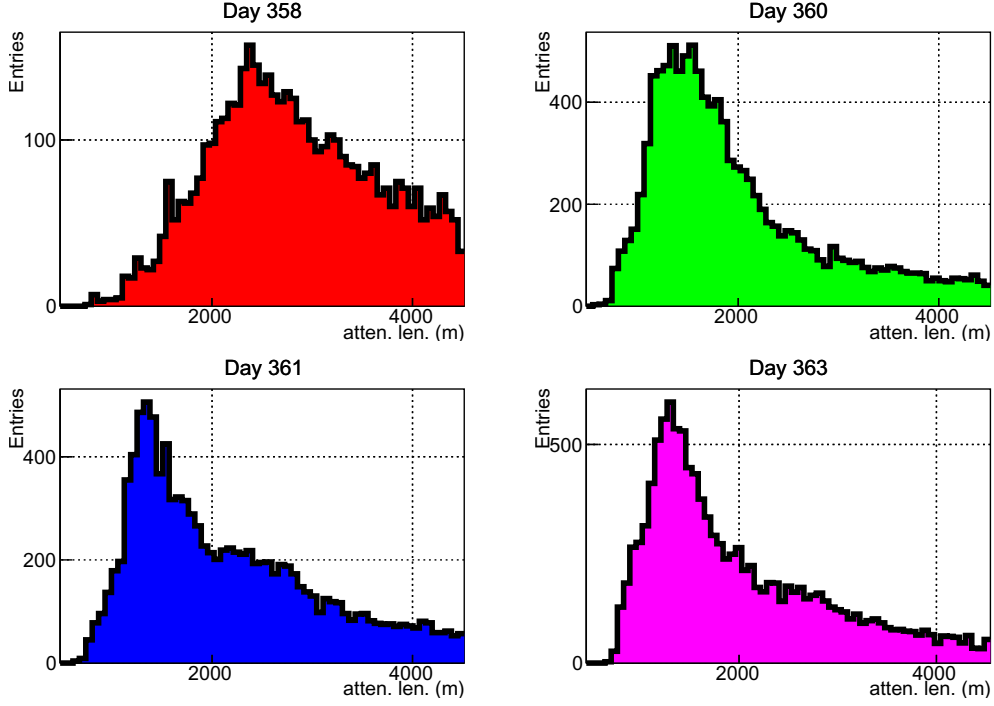
Figure 25. Attenuation length distribution based on SPICE core pulsing for indicated days. Derived attenuation lengths are $L_{atten} = 2377 \pm 645$ (Day 358), $L_{atten} = 1540 \pm 361$ (Day 360), $L_{atten} = 1348 \pm 383$ (Day 361), and $L_{atten} = 1302 \pm 372$ (Day 363), respectively. Shown errors represent width of peak region of distribution.

25, corresponding to peak values of L_{atten}=2377, 1540, 1348 and 1302 meters, respectively) show general consistency with attenuation length estimates extracted from the deep pulsers, and are consistent with previous >1 km cold-ice radio-frequency L_{atten} determinations[15, 39].

7   Systematics

The calculations described herein are based on signal amplitude and signal arrival time measurements extracted from ARA receiver waveforms. Quantifying the variation in these parameters is complicated by the intrinsic shot-to-shot variation in the SPUNK PVA transmitter output signal strength and signal width, measured to be ∼40%, and ∼35%, respectively, in pre-deployment testing, with signal width/amplitude showing a general increase/decrease over time. Loss of transmitter signal fidelity results in amplitude-dependent waveform slewing corresponding to approximately one nanosecond of uncertainty in the hit-time definition; both birefringence and $\delta_t(D, R)$ estimates therefore have systematic uncertainties of order two ns, as evident from Fig. 20. This uncertainty is also typical of saturated signals, since timing measurements are based on leading edges. Attenuation length measurements are additionally sensitive to event-by-event variation in measured signal strength for the ARA receiver stations. To isolate systematics at the receiver end, the effect of transmitter-dependent variations can be excluded by comparing the amplitudes and hit-times in two stations for the same transmitter output pulse – such events can be identified by requiring that the global trigger time for two station triggers are coincident to within 100 microseconds, corresponding

to 5× the scale of the maximum signal transit time between the ARA stations registering triggers. From such coincidences (and corroborated by the variation observed in local dedicated calibration pulsers), we estimate the intrinsic variation in the measured individual-channel receiver signal amplitude to be of order 20%. This value is smaller than the uncertainty in the channel-to-channel receiver gain, as evident from local calibration pulser signals.

The attenuation length distributions presented herein exhibit significant width. Monte Carlo simulations can be used to numerically interpret those widths. A simulation assuming infinite precision in measured signal amplitude, as expected, yields a delta-function for the extracted attenuation length distribution. We find that smearing our voltage amplitude distributions by a factor of 2.4±0.4 (with the error shown indicative of the range of values required to match observations for the four days shown), corresponding to an average voltage uncertainty of 3.8 dB, reproduces the width of the attenuation length distributions shown. We emphasize here that that value includes not only the uncertainty in the intrinsic antenna plus data-acquisition electronics, but also uncertainties introduced by propagation through ice from the SPUNK PVA to the receivers.

8   Summary and Conclusions

Data taken using either static, or movable radio-frequency transmitters at South Pole provide an excellent opportunity for radioglaciology measurements and provide essential information to in-ice neutrino detectors. Indeed, the SPICE core data sample described herein has very recently been used to test models of RF ice crystal geophysics[40], quantify the sensitivity of the ARA detector to cosmogenic neutrinos[41], and quantify the polarization response of the ARIANNA experiment[32]. Herein, we present results based on multi-kilometer propagation of radio-frequency signals broadcast through cold polar ice, with the goal of quantifying the impact on neutrino detection experiments. We find:

- From a measurement of the difference in signal arrival time between Direct and Refracted rays, we have derived a range of refractive index profiles which adequately fit the data. As shown elsewhere[13], this technique allows a range-to-vertex estimate with uncertainty of order 10-15%. The error in the extracted refractive index profile implies a corresponding uncertainty in neutrino effective volume of order 2-3%.

- Multiple measurements of the signal arrival time as a function of polarization ('birefringence') demonstrate, for horizontally propagating rays, a linear dependence of the birefringent asymmetry on range-to-vertex, once the signal incidence angle is determined by standard interferometric reconstruction techniques. Although ice birefringence presents additional challenges for data acquisition systems anticipated for next-generation radio arrays, by inverting this linear dependence, the observed HPol/VPol time-difference asymmetry, combined with the additional geometric leverage afforded by observation of both Direct and Refracted rays from an in-ice source also significantly improve the ability to estimate the range to an in-ice neutrino vertex, which is itself essential for a neutrino energy estimate. The range precision is geometry-dependent, and typically ≈15%.

- We demonstrate that cold polar ice has the long radio-frequency attenuation length needed for cosmic ray neutrino sensitivity. These measurements, for the first time, are conducted over the long horizontal baselines characteristic of neutrino signals, unlike previous vertical 'bounce' measurements.

With the cancellation of the 2020-21 South Polar field season, these are the last such measurements until such time as access to the SPICE core hole is restored; the timescale for those next measurements is uncertain.

Acknowledgments

References

References

[1] G. Askaryan. Excess negative charge of an electron-photon shower and its coherent radio emission. *Soviet Physics JETP*, 14:441–443, 1962.

[2] G. A. Askaryan. Excess negative charge of electron-photon shower and the coherent radiation originating from it. radiorecording of showers under the ground and on the moon. *J. Phys. Soc. Japan*, Vol. 17, Suppl. A-III:257, 1962.

[3] G. A. Askaryan. Coherent Radio Emission from Cosmic Showers in Air and in Dense Media. *Soviet Phys. JETP*, 21:658, 1965.

[4] I. Kravchenko, G. M. Frichter, D. Seckel, G. M. Spiczak, J. Adams, S. Seunarine, C. Allen, A. Bean, D. Besson, D. J. Box, R. Buniy, J. Drees, D. McKay, J. Meyers, L. Perry, J. Ralston, S. Razzaque, and D. W. Schmitz. Performance and simulation of the RICE detector. *Astropart. Phys.*, 19:15–36, April 2003.

[5] P. W. Gorham, P. Allison, S W. Barwick, and et al. The Antarctic Impulsive Transient Antenna ultra-high energy neutrino detector: Design, performance, and sensitivity for the 2006-2007 balloon flight. *Astropart. Phys.*, 32(1):10 – 41, 2009.

[6] P. Allison and J. Auffenberg and R. Bard and J. J. Beatty and D. Z. Besson and S. Boeser and C. Chen and P. Chen and A. Connolly and J. Davies and M. DuVernois and B. Fox and P. W. Gorham and E. W. Grashorn and K. Hanson and J. Haugen and K. Helbing and B. Hill and K. D. Hoffman and M. Huang and M. H. A. Huang and A. Ishihara and A. Karle and D. Kennedy and H. Landsman and A. Laundrie and T. C. Liu and L. Macchiarulo and K. Mase and T. Meures and R. Meyhandan and C. Miki and R. Morse and M. Newcomb and R. J. Nichol and

K. Ratzlaff and M. Richman and L. Ritter and B. Rotter and P. Sandstrom and D. Seckel and J. Touart and G. S. Varner and M.-Z. Wang and C. Weaver and A. Wendorff and S. Yoshida and R. Young. Design and Initial Performance of the Askaryan Radio Array Prototype EeV Neutrino Detector at the South Pole. *Astropart. Phys.*, 35:457–477, 2012.

[7] S. W. Barwick and E. C. Berg and D. Z. Besson and E. Cheim and T. Duffin and J. C. Hanson and S. R. Klein and S. A. Kleinfelder and T. Prakash and M. Piasecki and K. Ratzlaff and C. Reed and M. Roumi and A. Samanta and T. Stezelberger and J. Tatar and J. Walker and R. Young and L. Zou. Design and Performance of the ARIANNA Hexagonal Radio Array Systems. *IEEE Trans. Nucl. Sci.*, 62(5):2202–2215, 2015.

[8] Ilya Kravchenko, David Besson, and Josh Meyers. In situ index-of-refraction measurements of the south polar firn with the rice detector. *Journal of Glaciology*, 50(171):522–532, 2004.

[9] PW Gorham, P Allison, O Banerjee, L Batten, JJ Beatty, K Belov, DZ Besson, WR Binns, V Bugaev, P Cao, et al. The HiCal 2 Instrument: Calibration and Antarctic Surface Reflectivity Measurement for the ANITA Experiment. *arXiv preprint arXiv:1710.11175*, 2017.

[10] DZ Besson, J Jenkins, S Matsuno, J Nam, M Smith, SW Barwick, JJ Beatty, WR Binns, C Chen, P Chen, et al. In situ radioglaciological measurements near taylor dome, antarctica and implications for ultra-high energy (uhe) neutrino astronomy. *Astroparticle Physics*, 29(2):130–157, 2008.

[11] DZ Besson, J Stockham, M Sullivan, P Allison, JJ Beatty, K Belov, WR Binns, C Chen, P Chen, JM Clem, et al. Antarctic radio frequency albedo and implications for cosmic ray reconstruction. *Radio Science*, 50(1):1–17, 2015.

[12] S.W. Barwick and E.C. Berg and D. Besson and T. Duffin and J. C. Hanson and S.R. Klein and S.A. Kleinfelder and C. Reed and M. Roumi and T. Stezelberger and J. Tatar and J. Walker and L. Zou. Radio-frequency Attenuation Length, Basal-Reflectivity, Depth, and Polarization Measurements from Moore's Bay in the Ross Ice-Shelf. *J. Glaciol*, 61, 2015.

[13] P Allison, S Archambault, J Auffenberg, R Bard, JJ Beatty, M Beheler-Amass, DZ Besson, M Beydler, CC Chen, CH Chen, et al. Measurement of the real dielectric permittivity epsilon' of glacial ice. *Astroparticle Physics*, 108:63–73, 2019.

[14] Dave Besson, Ilya Kravchenko, Andres Ramos, and Juliet Remmers. Radio Frequency Birefringence in South Polar Ice and Implications for Neutrino Reconstruction. *Astropart. Phys.*, 34:755–768, 2011.

[15] Barwick, S and Besson, D and Gorham, P and Saltzberg, D. South Polar in situ radio-frequency ice attenuation. *Journal of Glaciology*, 51(173):231–238, 2005.

[16] R. Abbasi, M. Abou Bakr Othman, C. Allen, L. Beard, J. Belz, D. Besson, M. Byrne, B. Farhang-Boroujeny, A. Gardner, W.H. Gillman, W. Hanlon, J. Hanson, C. Jayanthmurthy, S. Kunwar, S.L. Larson, I. Myers, S. Prohyra, K. Ratzlaff, P. Sokolsky, H. Takai, G.B. Thomson, and D. Von Maluski. Telescope Array Radar (TARA) Observatory for Ultra-High Energy Cosmic Rays. *Nucl. Instrum. Meth.*, A767:322–338, 2014.

[17] J. Abraham, M. Aglietta, I. C. Aguirre, M. Albrow, D. Allard, I. Allekotte, P. Allison, and et al. Properties and performance of the prototype instrument for the Pierre Auger Observatory. *Nucl. Instrum. Meth.*, A523:50–95, 2004.

[18] K. Greisen. End to the Cosmic-Ray Spectrum? *Phys. Rev. D*, 16:748–750, 1966.

[19] G.T. Zatsepin and V.A. Kuz'min. Upper Limit of the Spectrum of Cosmic Rays. *JETP Letters*, 4:78–80, 1966.

[20] V.S. Berezinsky and G.T. Zatsepin. On the origin of cosmic rays at high energies. *Phys. Lett. B*, 28:423, 1969.

[21] P Allison, S Archambault, R Bard, JJ Beatty, M Beheler-Amass, DZ Besson, M Beydler, M Bogdan, C-C Chen, C-H Chen, et al. Design and performance of an interferometric trigger array for radio detection of high-energy neutrinos. *Nuclear Instruments and Methods in Physics Research Section A: Accelerators, Spectrometers, Detectors and Associated Equipment*, 930:112–125, 2019.

[22] SW Barwick, EC Berg, DZ Besson, G Gaswint, C Glaser, A Hallgren, JC Hanson, SR Klein, S Kleinfelder, L Köpke, et al. Observation of classically forbidden'electromagnetic wave propagation and implications for neutrino detection. *arXiv preprint arXiv:1804.10430*, 2018.

[23] C Deaconu, AG Vieregg, SA Wissel, J Bowen, S Chipman, A Gupta, C Miki, RJ Nichol, and D Saltzberg. Measurements and modeling of near-surface radio propagation in glacial ice and implications for neutrino experiments. *arXiv preprint arXiv:1805.12576*, 2018.

[24] Kimberly Ann Casey, TJ Fudge, TA Neumann, EJ Steig, MGP Cavitte, and DD Blankenship. The 1500 m South Pole ice core: recovering a 40 ka environmental record. *Annals of Glaciology*, 55(68):137–146, 2014.

[25] Jean-Robert Petit, Jean Jouzel, Dominique Raynaud, Narcisse I Barkov, J-M Barnola, Isabelle Basile, Michael Bender, J Chappellaz, M Davis, G Delaygue, et al. Climate and atmospheric history of the past 420,000 years from the vostok ice core, antarctica. *Nature*, 399(6735):429, 1999.

[26] Fabrice Lambert, Barbara Delmonte, Jean-Robert Petit, Matthias Bigler, Patrick R Kaufmann, Manuel A Hutterli, Thomas F Stocker, Urs Ruth, Jørgen Peder Steffensen, and Valter Maggi. Dust-climate couplings over the past 800,000 years from the epica dome c ice core. *Nature*, 452(7187):616, 2008.

[27] Joan J Fitzpatrick, Donald E Voigt, John M Fegyveresi, Nathan T Stevens, Matthew K Spencer, Jihong Cole-Dai, Richard B Alley, Gabriella E Jardine, Eric D Cravens, Lawrence A Wilen, et al. Physical properties of the wais divide ice core. *Journal of Glaciology*, 60(224):1181–1198, 2014.

[28] George P Rigsby. Crystal orientation in glacier and in experimentally deformed ice. *Journal of Glaciology*, 3(27):589–606, 1960.

[29] PW Gorham, P Allison, O Banerjee, JJ Beatty, K Belov, DZ Besson, WR Binns, V Bugaev, P Cao, C Chen, et al. Antarctic Surface Reflectivity Measurements from the ANITA-3 and HiCal-1 Experiments. *Journal of Astronomical Instrumentation*, page 1740002, 2017.

[30] S Prohira, A Novikov, P Dasgupta, P Jain, S Nande, P Allison, O Banerjee, L Batten, JJ Beatty, K Belov, et al. Antarctic surface reflectivity calculations and measurements from the anita-4 and hical-2 experiments. *Physical Review D*, 98(4):042004, 2018.

[31] S Prohira, A Novikov, DZ Besson, K Ratzlaff, J Stockham, M Stockham, JM Clem, R Young, PW Gorham, P Allison, et al. Hical 2: An instrument designed for calibration of the anita experiment and for antarctic surface reflectivity measurements. *Nuclear Instruments and Methods in Physics Research Section A: Accelerators, Spectrometers, Detectors and Associated Equipment*, 918:60–66, 2019.

[32] A Anker, SW Barwick, H Bernhoff, DZ Besson, N Bingefors, D García-Fernández, G Gaswint, C Glaser, A Hallgren, JC Hanson, et al. Probing the angular and polarization reconstruction of the arianna detector at the south pole. *arXiv preprint arXiv:2006.03027, and in press at Journal of Cosmology and Astroparticle Physics*, 2020.

[33] AG Vieregg, K Bechtol, and A Romero-Wolf. A technique for detection of pev neutrinos using a phased radio array. *Journal of Cosmology and Astroparticle Physics*, 2016(02):005, 2016.

[34] KARL C Kuivinen. A 237-meter ice core from south pole station. *Antarct. J. US*, 18(5):113–114, 1983.

[35] Michiel van den Broeke. Depth and density of the antarctic firn layer. *Arctic, Antarctic, and Alpine Research*, 40(2):432–438, 2008.

[36] P Buford Price, Oleg V Nagornov, Ryan Bay, Dmitry Chirkin, Yudong He, Predrag Miocinovic, Austin Richards, Kurt Woschnagg, Bruce Koci, and Victor Zagorodnov. Temperature profile for glacial ice at the South Pole: Implications for life in a nearby subglacial lake. *Proceedings of the National Academy of Sciences*, 99(12):7844–7847, 2002.

[37] D. Besson, R. Keast, and R. Velasco. In situ and laboratory studies of radiofrequency propagation through ice and implications for siting a large-scale Antarctic neutrino detector. *Astropart. Phys.*, 31:348–358, 2009.

[38] Shuji Fujita, Hideo Maeno, and Kenichi Matsuoka. Radio-wave depolarization and scattering within ice sheets: a matrix-based model to link radar and ice-core measurements and its application. *Journal of Glaciology*, 52(178):407–424, 2006.

[39] P. Allison and J. Auffenberg and R. Bard and J. J. Beatty and D. Z. Besson and S. Boeser and C. Chen and P. Chen and A. Connolly and J. Davies and M. DuVernois and B. Fox and P. W. Gorham and E. W. Grashorn and K. Hanson and J. Haugen and K. Helbing and B. Hill and K. D. Hoffman and M. Huang and M. H. A. Huang and A. Ishihara and A. Karle and D. Kennedy and H. Landsman and A. Laundrie and T. C. Liu and L. Macchiarulo and K. Mase and T. Meures and R. Meyhandan and C. Miki and R. Morse and M. Newcomb and R. J. Nichol and K. Ratzlaff and M. Richman and L. Ritter and B. Rotter and P. Sandstrom and D. Seckel and J. Touart and G. S. Varner and M.-Z. Wang and C. Weaver and A. Wendorff and S. Yoshida and R. Young. Design and initial performance of the Askaryan Radio Array prototype EeV neutrino detector at the South Pole. *Astroparticle Physics*, 35(7):457–477, 2012.

[40] TM Jordan, DZ Besson, I Kravchenko, U Latif, B Madison, A Nokikov, and A Shultz. Modeling ice birefringence and oblique radio wave propagation for neutrino detection at the south pole. *Annals of Glaciology*, pages 1–8, 2019.

[41] P Allison, S Archambault, JJ Beatty, M Beheler-Amass, DZ Besson, M Beydler, CC Chen, CH Chen, P Chen, BA Clark, et al. Constraints on the diffuse flux of ultra-high energy neutrinos from four years of askaryan radio array data in two stations. *arXiv preprint arXiv:1912.00987, and accepted by Phys. Rev. D.*, 2019.